

Multipurpose On-the-Spot Peptide-Based Hydrogels for Skin, Cornea, and Heart Repair

Alex Ross, Xixi Guo, German A. Mercado Salazar, Sergio David Garcia Schejtman, Jinane El-Hage, Maxime Comtois-Bona, Aidan Macadam, Irene Guzman-Soto, Hiroki Takaya, Kevin Hu, Bryan Liu, Ryan Tu, Bilal Siddiqi, Erica Anderson, Marcelo Muñoz, Patricio Briones-Rebolledo, Tianqin Ning, May Griffith, Benjamin Rotsein, Horacio Poblete, Jianyu Li, Marc Ruel,* Erik J. Suuronen,* and Emilio I. Alarcon*

Bioinspired synthetic materials can be designed as reliable, cost-effective, and fully controlled alternatives to natural biomaterials for treating damaged tissues and organs. However, several hurdles need to be overcome for clinical translation, particularly for biomaterials gelled in situ. These include the potential toxicity of chemical crosslinkers used in the materials' assembly or breakdown products they generate and the challenges of fine-tuning the mechanical properties of the materials. Here, a minimalistic, adhesive soft material is developed by screening hundreds of potential formulations of self-assembling, custom-designed collagen-like peptide sequences for the in situ formation of tissue-bonding 3D hydrogels. Nine promising formulations for tissue repair are identified using a low-volume and rapid combinatorial screening approach. It is shown that simply varying the ratio of the two key components promotes adhesion and fine-tunes the material's mechanical properties. The materials' skin and heart repair capabilities are assessed in vitro and clinically relevant animal models. The materials are also tested for corneal applications using ex vivo pig cornea models complemented by in vitro cell compatibility assays.

1. Introduction

Historically, extracted natural polymers have been widely used as building blocks for the synthesis of materials with therapeutic potential for organ and tissue repair.^[1] While some of these materials are already in clinical use,^[2–6] the lack of precise chemical tunability, batch-to-batch variability, generally weak mechanical properties, and potential immunogenicity stemming from biological impurities and pathogen transfer remain barriers to biomedical innovation.^[7–9] Further, the concept of “one size fits all” is unrealistic, when considering the intrinsic differences in physical and mechanical properties amongst organs and tissues, as well as the variance between individuals in the shape and extent of tissue damage in need of repair.^[10] Thus, in recent years, the use of synthetic materials,^[11] whose properties can be finely tuned, has

A. Ross, X. Guo, G. A. M. Salazar, S. D. G. Schejtman, J. El-Hage, M. Comtois-Bona, A. Macadam, I. Guzman-Soto, H. Takaya, K. Hu, B. Liu, R. Tu, B. Siddiqi, E. Anderson, M. Muñoz, M. Ruel, E. J. Suuronen, E. I. Alarcon
Bioengineering and Therapeutic Solutions (BEaTS) program
University of Ottawa Heart Institute
40 Ruskin Street, Ottawa, Ontario K1Y4W7, Canada
E-mail: mrue@ottawaheart.ca; esuuronen@ottawaheart.ca; earlaron@uottawa.ca

A. Ross, G. A. M. Salazar, B. Rotsein, E. I. Alarcon
Department of Biochemistry
Microbiology
and Immunology
University of Ottawa
Ottawa, Ontario K1H 8M5, Canada

 The ORCID identification number(s) for the author(s) of this article can be found under <https://doi.org/10.1002/adfm.202402564>

© 2024 The Authors. Advanced Functional Materials published by Wiley-VCH GmbH. This is an open access article under the terms of the [Creative Commons Attribution-NonCommercial](https://creativecommons.org/licenses/by-nc/4.0/) License, which permits use, distribution and reproduction in any medium, provided the original work is properly cited and is not used for commercial purposes.

DOI: 10.1002/adfm.202402564

X. Guo, E. J. Suuronen
Department of Cellular & Molecular Medicine
University of Ottawa
451 Smyth Road, Ottawa, Ontario K1H8M5, Canada

P. Briones-Rebolledo, H. Poblete
Departamento de Bioinformática
Centro de Bioinformática
Simulación y Modelado (CBSM)
Facultad de Ingeniería
Universidad de Talca
Campus Talca, 2 Norte 685, Talca 75710, Chile

T. Ning
Department of Mechanical Engineering
McGill University
Montreal, Quebec H3A0C3, Canada

M. Griffith, J. Li
Department of Ophthalmology and Institute of Biomedical Engineering
Université de Montréal
Montreal, Quebec H3C3J7, Canada

gained considerable interest, with successful examples in soft tissue organ repair.^[12] Among many possible synthetic materials, short peptide-based (<50 amino acids long) materials have several advantages including their capacity to mimic the biological functions of their full-length counterparts, the flexibility for further chemical modification, as exemplified by β -sheet-forming self-assembling peptides, and the relatively low cost of manufacturing at clinical grade.^[13,14] However, to obtain stronger 3D peptide materials, potentially toxic chemical crosslinkers such as carbodiimide or polymerization catalysts are often used, which can result in detrimental effects in cell and tissue regeneration.^[15–17] Thus, using pre-crosslinked materials where side-products have been removed prior to implantation remains the norm.^[18] Further, it is imperative that the design of peptide sequences encompasses supramolecular self-assembly of the chains in the crosslinked state to strengthen the resulting mechanical properties of the final material product. An example of this is the reported bio-orthogonal assembly of peptide-based hydrogels, mainly using single cysteine containing peptides.^[19–21] In another approach, PEG-maleimide conjugation with collagen-like peptides (CLPs) using a short cysteine containing amino acid linker was used to generate corneal implants.^[22] CLPs mimic the tertiary structure of collagen, a structural protein that provides strength to tissues, and is often composed of Glycine-Proline-Proline (GPP) or Glycine-Proline-Hydroxyproline (GPO) amino acid triplets.^[23]

Herein, we used a low-volume rapid screening approach to identify candidate self-assembling peptide structures for building adhesive biomaterials with tunable mechanical properties ranging from 1 to 100 kPa in strength. The peptide sequences contain a glycine-flanked cysteine at each of the peptide ends. As a polymeric backbone, we used polyethylene glycol (PEG), an FDA approved synthetic polymer,^[24] with demonstrated safety and stability.^[25] Long chain- multi-armed PEG structures bearing terminal maleimides were used to form polymeric networks. Using a Michael-addition reaction between maleimide and sulfhydryl groups at physiological pH results in the rapid formation of adhesive 3D-structures with tunable mechanical properties. This material design combines the dual mechanisms of chemical bonding and molecular assembly that are often used in nature to provide tissues with mechanical stability.^[26] This chemistry also minimizes potential cross-reactions when used in vivo compared to other chemical groups such as acrylamides,^[27] and yields stable bonds (>2 years).^[28]

While the concept of peptide-PEG on-the-spot assembly sounds simple in principle, there are many structural and chemical considerations, which in practice may require challenging peptide synthesis. Our study design, based on using a low-volume screening process, allowed for the testing of +200 formulations (+20 peptide sequences) to identify the best candidate peptide for on-the-spot tissue repair. Optimal peptide sequences were identified as those that: (1) Formed a triple helix in solution and showed stability at physiological pH and temperature; (2) showed suitable gelation times, e.g., 15–120s; and (3) formed 3D materials with suitable physical properties for use in soft tissue repair (e.g., transmittance, refractive index, denaturation temperature, water content, and resistance to collagenase degradation). Crude purity was also considered in the selection process as it is critical for scale up in future clinical translation.

2. Results

2.1. Peptide Engineering and Validation

Collagen is the most abundant protein in the human body and is present in most tissues and organs, spanning from bones to highly vascularized tissues such as the heart.^[29] With 28 different identified types, the mechanical properties of collagens are as diverse as the tissues they support.^[29] The versatility of collagen as a scaffold protein is a consequence of its unique nanosized triple helical structure formed by three collagen polypeptide chains, and how this supramolecular structure can further macro-assemble.^[30] Mimicking the trimer assembly mechanism of collagen is possible by using CLPs.^[23] In CLPs, the amino acid trimer sequence proline-hydroxyproline-glycine (POG) is well-known to yield a triple helical structure when >4 repeats are present.^[30,31] However, the triple helix formation is a dynamic process, which in some cases is favoured by attachment of a CLP to a polymeric structure.^[23]

The peptide library that we generated included a total of 21 CLP sequences plus a collagen peptide structure that has been previously used for developing implantable corneas (see Table 1).^[22] Using POG as a repetitive unit allows for the greatest stabilization of the collagen triple helix among the repetitive units found in nature.^[32] The range of peptide sequences synthesized spanned from 18 to 38 amino acids (see Table S1, Supporting Information for mass spectrometry data and crude purity). To minimize steric repulsion and increase reactivity in peptides containing cysteines, unless otherwise mentioned, each cysteine residue was flanked by two flexible glycine residues that allowed the sulfhydryl group to move in space.^[33] Further, in designing the peptide sequences, we avoided using terminal cysteines as they could make synthesis challenging and increase the cost.^[34] Thus, the GCG motif was added to each end of the peptide sequences with the repetitive POG unit, from (POG)₄Pep-1 (18 amino acids) to (POG)₁₀Pep-7 (36 amino acids; see Table 1). Notably, the addition of two cysteine residues did not result in significant formation of dimers in solution (Figure S1, Supporting Information). The available number of cysteines in phosphate buffer (pH 7.4) was found to be similar between our peptides and free Cys (>90%) (see Figure S2, Supporting Information for a representative example). We began by assessing the effect of peptide length on the CLPs' ability to form triple helices stable at human physiological temperature (Table 1). Analysis of the melting curves indicated that, as expected, increasing the sequence length resulted in cooperative melting transitions (Figure S3, Supporting Information). To assess the functional impact of changes in the peptide sequence on 3D structure assembly when using nucleophilic Michael-addition to PEG-maleimide, a series of peptide sequences were designed and synthesized using Pep-5 as a building block as it is cost-effective, has >70% crude yield (Table S1, Supporting Information), and displayed a cooperative melting behavior (Figure S3, Supporting Information). Table 1 summarizes the main modifications for this group of peptide sequences (Pep-8 to Pep-21).

We used the R_{pn} parameter ($R_{pn} = 225 \text{ nm}/200 \text{ nm}$ circular dichroism signal), to differentiate between the triple-helix conformation and the poly(Pro)-II helix conformation.^[35,36] Poly(Pro)-II helix conformations show very low R_{pn} values (<0.005),^[35] and

Table 1. Sequences, including structural features, ellipticity, and denaturation temperature for peptide sequences prepared in this study. Further characterization of the peptides can be found in the Supplementary Information (Table S1, Supporting Information). To facilitate visualization of the structural changes carried out, POG repetitive sequences and C residues are bolded in black and red, respectively.

Sample	Sequence	Sequence structural features	R _{pn} value ^{a)}	T _m [°C] ^{b)}
Pep-1	H-GCC(POG) ₄ GCG-OH	4 POG repetitive units containing two glycine flanking cysteines at each end	0.032 ± 0.005	44.1 ± 0.8
Pep-2	H-GCC(POG) ₅ GCG-OH	5 POG repetitive units containing two glycine flanking cysteines at each end	0.034 ± 0.001	49.0 ± 1.0
Pep-3	H-GCC(POG) ₆ GCG-OH	6 POG repetitive units containing two glycine flanking cysteines at each end	0.072 ± 0.008	52.0 ± 2.0
Pep-4	H-GCC(POG) ₇ GCG-OH	7 POG repetitive units containing two glycine flanking cysteines at each end	0.084 ± 0.003	54.1 ± 0.4
Pep-5	H-GCC(POG) ₈ GCG-OH	8 POG repetitive units containing two glycine flanking cysteines at each end	0.087 ± 0.002	59.0 ± 3.0
Pep-6	H-GCC(POG) ₉ GCG-OH	9 POG repetitive units containing two glycine flanking cysteines at each end	0.094 ± 0.002	64.0 ± 4.0
Pep-7	H-GCC(POG) ₁₀ GCG-OH	10 POG repetitive units containing two glycine flanking cysteines at each end	0.094 ± 0.001	65.0 ± 6.0
Pep-8	H-GGG(POG) ₈ GCG-OH	Replacing amino terminal cysteine with glycine in the 8 POG repetitive containing sequence	0.113 ± 0.001	61.9 ± 0.4
Pep-9	H-GCG(POG) ₈ GGG-OH	Replacing carboxy terminal cysteine with glycine in the 8 POG repetitive containing sequence	0.118 ± 0.002	49.4 ± 0.2
Pep-10	H-GGG(POG) ₈ GGG-OH	Replacing both cysteines with glycine in the 8 POG repetitive containing sequence	0.120 ± 0.002	55.9 ± 0.2
Pep-11	H-GGG(POG) ₃ (PCG) ₂ (POG) ₃ GGG-OH	Cysteine shift to middle of sequence in the 8 POG repetitive containing sequence	0.054 ± 0.002	43.1 ± 0.7
Pep-12	H-GGG(POG) ₂ (PCG)(POG) ₅ GCG-OH	Amino terminal cysteine shift to center of sequence in the 8 POG repetitive containing sequence	0.078 ± 0.001	50.7 ± 0.3
Pep-13	H-GCG(POG) ₃ (PCG)(POG) ₂ GGG-OH	Carboxy terminal cysteine shift to center of the 8 POG repetitive containing sequence	0.091 ± 0.001	50.5 ± 0.3
Pep-14	H-GGG(POG) ₂ (PCG)(POG) ₂ (PCG)(POG) ₂ GGG-OH	Both cysteine shift to center of sequence in the 8 POG repetitive containing sequence	0.074 ± 0.003	39.0 ± 0.3
Pep-15	H-GCC(POG) ₄ POV(POG) ₃ GCG-OH	Disrupting folding by replacing one POG by POV at the center of the sequence in the 8 POG repetitive containing sequence	0.028 ± 0.001	45.0 ± 2.0
Pep-16	H-GCC(PPG) ₈ GCG-OH	Disrupting folding by replacing hydroxyproline with proline in the 8 POG repetitive containing sequence	0.007 ± 0.001	43.0 ± 2.0
Pep-17	H-GC(POG) ₈ CG-OH	Removing glycine spacer in the 8 POG repetitive containing sequence	0.080 ± 0.002	58.0 ± 2.0
Pep-18	H-GCV(POG) ₈ VCG-OH	Replacing glycine with valine as spacer in the 8 POG repetitive containing sequence	0.055 ± 0.001	54.0 ± 2.0
Pep-19	H-GCR(POG) ₈ RCG-OH	Replacing glycine with arginine as spacer in the 8 POG repetitive containing sequence	0.081 ± 0.001	60.0 ± 2.0
Pep-20	H-GCC(POG) ₈ CCG-OH	Multiple cysteine residues at both ends in the 8 POG repetitive containing sequence	0.062 ± 0.001	51.4 ± 0.6
Pep-21	H-GCC(POG) ₂ (PCG)(POG) ₂ (PCG)(POG) ₂ GCG-OH	Multiple cysteine residues at ends and middle in the 8 POG repetitive containing sequence	0.055 ± 0.003	47.9 ± 0.3
CLP	H-CG(PKG) ₄ (POG) ₄ (DOG) ₄ -OH	Control peptide	0.071 ± 0.009	42.0 ± 1.0

^{a)} Peptides concentration: 200 μM; PBS is phosphate buffered saline (1.0 mM) pH 7.4 at 25 °C; ^{b)} Representative melting curves are included in Figure S3 (Supporting Information).

collagen displays R_{pn} values ≈0.12.^[35] Pep-1 to Pep-8 presented R_{pn} values ≥ 0.035±0.004, which corresponds to ≈50% of the R_{pn} value measured for the CLP control sequence (≈0.071). Further, the structural G-X-G(POG)_nG-X-G motif, with X being G or C, and n>7 results in R_{pn} values larger (0.087–0.084) than those measured for the control CLP. Upon screening of the different

lengths, sequences Pep-5 and Pep-6 showed the best ellipticity and higher denaturation temperature. The need for having the structural POG repetitive unit to yield highly elliptical peptides is illustrated when the POG repetitive unit is replaced with POV (Pep-15) or PPG (Pep-16), for example. In peptides whose peptide ellipticity is disrupted, such as Pep-15 that bears a single

G to V substitution, there is no cooperative denaturation behavior, which aligns well with the low R_{pn} value of 0.028. Similar results were observed for Pep-16, which has the lowest R_{pn} value (0.007) of the peptides synthesized. We also observed that peptides, such as Pep-5, increase their R_{pn} value as a function of the peptide concentration, similar to the control peptide CLP (Figure S4, Supporting Information). Further, the presence of cysteine decreases the peptide packing as showed by comparing the ellipticity of Pep-5 versus Pep-10. Molecular dynamics calculations suggest that Pep-5 does present a divergent packing when compared to the rest of the peptides screened, which might be the result of the presence of cysteine and the length of the POG chain (see Figure S5, Supporting Information). Root Mean Square Fluctuation analysis (Figure S6, Supporting Information) reveals the positional fluctuations of each peptide residue throughout the molecular dynamics. The peptides were grouped by the chain length, underscoring that Pep-5 exhibits a higher fluctuation at the top-end (residues 1–5), where the cysteine amino acid is contained. However, despite this fluctuation, Root Mean Square Deviation (Figure S6, Supporting Information) analysis of the entire peptide over the simulation time demonstrates high structural stability in all peptides, indicating for Pep-5 that this open conformation at the upper end is kept over time.

In summary, our foundational peptide sequences, in particular Pep-1 to Pep-8, present suitable self-assembling properties for testing their ability to form on-the-spot hydrogels for soft tissue and organ applications. In the next section, we will present the rationale and main findings for the preparation and testing of hydrogels using the peptide library developed herein.

2.2. Fabrication of 3D Materials for Soft Tissue Repair

The hydrogel design is based on a multi-arm polyethylene PEG polymer bio-orthogonally in situ crosslinked with engineered self-assembling peptides. PEG is a hydrophilic, cytocompatible polymer approved by the FDA for human use and thus represents an excellent base material for clinically translatable biomaterials.^[24,37,38] As the PEG molecule itself possesses little chemical reactivity, we used a multi-armed maleimide functionalized (PEG-maleimide) version of this polymer to allow in situ assembling into a 3D material. Among the possible functional groups, maleimide was chosen as it is an electrophilic Michael-addition acceptor with a superior kinetic profile compared to other commonly used groups such as acrylamide.^[27] Rapid kinetics are important to create a gel within a clinically relevant timeframe and to ensure complete reactivity to minimize cross-reactions upon application to the tissue.

Considering the different nucleophilic Michael-addition donors that can react with our PEG-maleimide, sulfhydryl groups possess rapid reaction kinetics and selectively form a stable Michael adduct,^[27] allowing for the creation of a stable hydrogel that is quickly formed. The natural amino acid cysteine contains a reactive sulfhydryl group^[39] and is thus chosen for incorporation into the peptide design as outlined in Table 1. Considering the peptide sequences used in this work, which include two cysteines in each strand, the click reaction with maleimides can yield up to two PEG-maleimides per strand. If the assembly of three CLP monomers alone can bring together three strands,

the reaction of this triple helix-like structure could yield up to six different PEG-maleimides per helix. This creates unique network dynamics that we show to result in the rapid formation of a durable, cytocompatible gel for tissue engineering. Note that these large trimer structures can be sterically hindered, and thus removal of the glycine spacer residues results in less efficient tissue bonding (Figure S7, Supporting Information).

Figure 1A shows a simplified schematic of the peptide-PEG assembly using our bi-functional peptides in combination with the multi-armed PEG maleimide. This figure also contains an overview of the low volume and rapid screening strategy we used for identifying the most promising peptide candidates. First, we monitored the stability of the PEG-maleimide in carbonate buffers (Figure S8, Supporting Information). As expected, the maleimide has moderate stability at pH 7.4. However, at low temperatures ($\approx 4.0^\circ\text{C}$) it is stable for up to 90 min. Thus, the experimental design kept the reagent solution on ice until it is applied and warmed up to physiological temperature. Furthermore, having the hydrogels formed within 1/10th of the half-life of the maleimide in solution (i.e., < 5 min) was used to minimize potential side reactions. We next screened the peptides' capacities to form hydrogels (see Figure S9, Supporting Information for a representative example). In preparing our materials, we used three different peptide:PEG-maleimide ratios (CM_{ratio}) of 1.0, 3.0, and 4.0. Thus, for example, for peptides bearing two cysteines, the CM_{ratio} 4.0 corresponds to materials where maleimides and cysteine residues are equimolar.

To select peptides that would allow for rapid in situ gelation, we first set a gelation time cut-off at a maximum of 120s, with any formulations (CM_{ratio} 1.0, 3.0, or 4.0) exhibiting longer gelation times removing the peptide from further consideration. Furthermore, we set a minimum of 15s to allow for some time to manipulate the solution into an appropriate form before it solidifies; see Figure 1B whereby heatmaps are used to illustrate the findings. These cut-offs (seen as <15s, beige, and >120s, dark blue) reduced the number of peptide candidates to 7, as some peptides, such as peptides 8–10 with <2 cysteine residues per molecule, would gel very slowly and other candidates, such as peptides 19–20 with >2 cysteine residues per molecule, would gel very quickly (<15s). Figure 1B also depicts representative images of small drops (50 μL) of the formulations prepared at CM_{ratio} 4.0 on a 22.5° inclined surface taken at different timepoints; 0s, 30s, and 45s (additional details in Materials and Methods). The images illustrate that the material prepared using Pep-10 remains viscous for +30s compared to the Pep-5 that rapidly becomes a gel (≈ 30 s). We also measured gelation time using water applied with a nebulizer to create a wet surface. The gelation time measured on a wet surface (20 ± 11 s) was significantly faster than on the dry surface (55 ± 28 s) and comparable to the CM_{ratio} 1.0 gelation time (33 ± 1.0 s), one-way ANOVA. The alteration in measured gelation time is likely due to a combination of the surface water diluting the solution to achieve an effective lower CM_{ratio} as well as the surface properties of the glass slide being altered by the presence of water.

Target values for other evaluated parameters (also illustrated using heat maps) include: transmittance > 85%, comparable to human cornea (Figure 1C);^[40] thus removing peptides 6, 7, and 17 from consideration. A refractive index < 1.380, similar to human cornea (Figure 1D), was used as additional criteria for

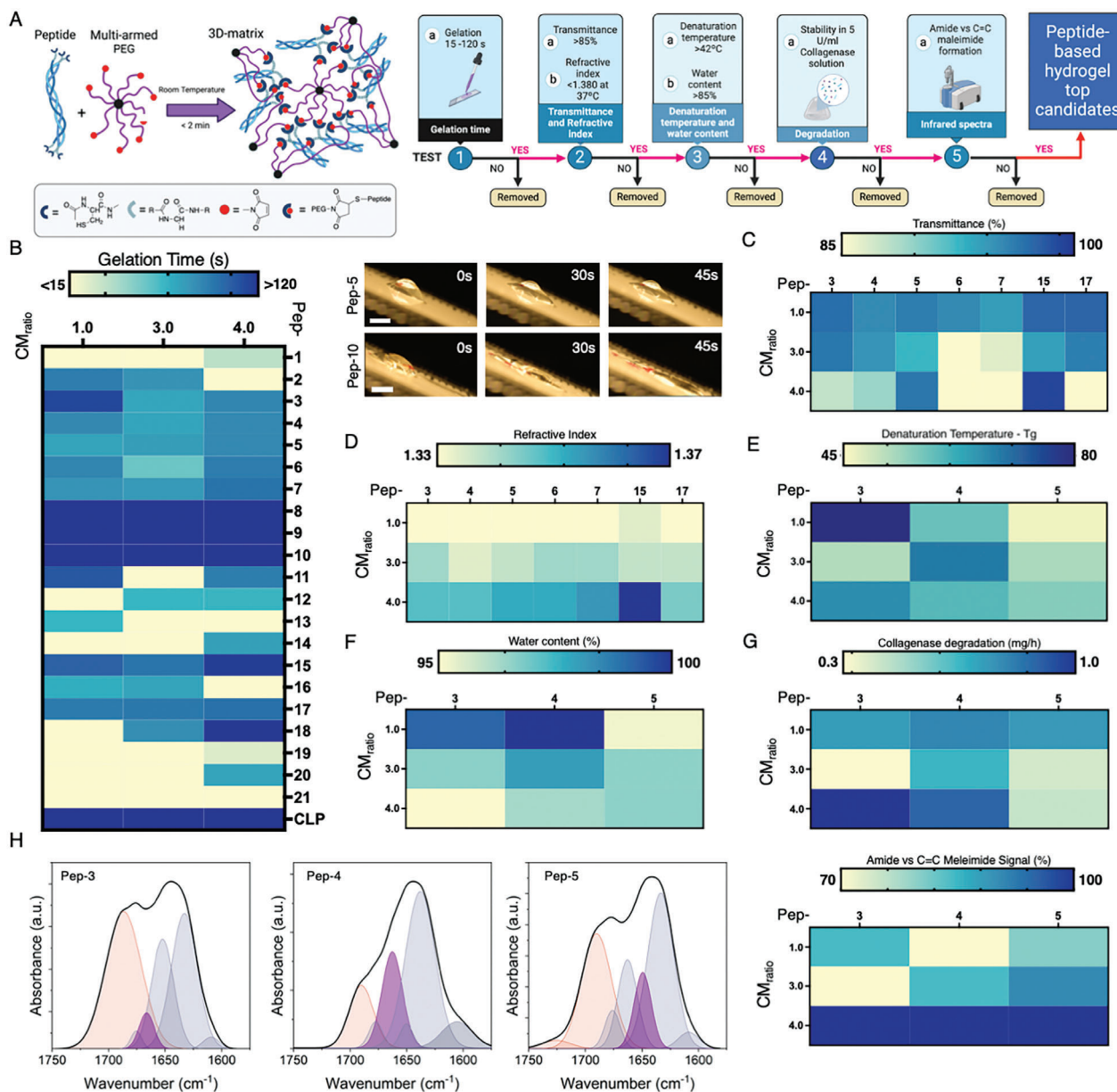


Figure 1. Engineered peptides for on-the-spot soft tissue repair. **A**) *Left*: Schematic depiction for the strategy used in this study for the in situ assembling of the materials. Assembly of the hydrogel takes place within minutes at room temperature. Some of the key chemical motifs of the material components are depicted at the bottom of the schematic. *Right*: Flow diagram showing the tests used to screen material formulations. This methodology was designed to narrow down the number of candidate formulations. **B–H**) Heatmaps are used to display changes in the properties measured following the schematic in Figure 1A. Each figure contains a colour scale illustrating changes in the parameters of materials with different CM_{ratio} and peptide formulations (abbreviated as Pep, raw data available in Table S2 (Supporting Information), $n = 5$) for: **(B)** *Left*: gelation time (s) and *Right*: Representative still images of two selected peptide formulations (50 μL , CM_{ratio} of 4.0) taken at 0, 30, and 45 s after positioning the samples at a 45° inclination. Scale bar is 2 mm; **(C)** Transmittance (%); **(D)** refractive index; **(E)** denaturation temperature ($^{\circ}\text{C}$); **(F)** water content (%); **(G)** collagenase degradation (mg h^{-1}); and **(H)** *Left*: ATR-FTIR (with the respective deconvoluted Gaussian fit) spectra of selected peptides at CM_{ratio} 1.0, where the light blue peaks correspond to the different Amide I signal of each peptide, and the light red and violet peaks correspond to the C = O and C = C of PEG-MAL, respectively. Experimental details are in the Materials and Methods and the Supplementary Information.

selection;^[41] thus peptide 15 was eliminated. Additional parameters include: a denaturation temperature $\geq 45^{\circ}\text{C}$, which is the highest temperature ever measured in a human (Figure 1E);^[42] water content $>60\%$, a value that covers soft organs such as skin, cornea, and heart in human adults (Figure 1F);^[43,44] and stability

in type I collagenase solution, i.e., degradation of $<5.0\text{ mg h}^{-1}$ which is the degradation rate for a 1.0% collagen hydrogel in solution (Figure 1G). FTIR analysis for the best hydrogel candidates was also carried out using a Gaussian fit of the Amide I region and compared with the pure peptides. On top of the

assignment for each signal (see Supporting Information for more details), a new peak that appears at 1650–1675 cm^{-1} could be attributed to unreacted C = C of the PEG-MAL molecule at a given CM_{ratio} . Comparing the hydrogels prepared with Pep-3 (Figure S10, Supporting Information), Pep-4 (Figure S11, Supporting Information), and Pep-5 (Figure S12, Supporting Information) at different CM_{ratio} , we estimated peptide to PEG-MAL reactivity, giving a higher relative area percent of Amide I/C = C signal for those formulations. Figure 1H shows the Gaussian fit for the Pep-3, Pep-4, and Pep-5 hydrogels at CM_{ratio} 1.0. This data indicates good agreement with the expected equimolar ratios of maleimide and thiols for the CM_{ratio} 4.0, meaning that the C = C signal is mostly absent and replaced by amide, suggesting a complete reaction. Table S2 (Supporting Information) displays the tabulated data for the heatmap plot results shown in Figure 1B–F.

In summary, our low volume rapid screening process allowed us to reduce the number of potential peptide-based formulations from ≈ 200 (each formulation repeated at least in triplicate) to only 9 top formulations with peptides 3, 4, and 5 as primary candidates for further testing.

As mentioned, this initial screening process allowed us to narrow down three top peptides as primary candidates for hydrogel preparation (Pep-3, –4, and –5) at three different CM_{ratio} . Since we aim to apply/deliver the materials directly to the tissue, we chose buffers that allow for fast reaction in a pH range safe for cells, such as bicarbonate or Hanks buffer (pH 7.0).^[45] The materials showed hydrogel formation using all the buffers tested (see representative example in Figure S9, Supporting Information). Further, since our goal is to develop a clinically translatable material, we optimized the physical properties of the material prior to hydrogel formation to make them deliverable via a ≈ 400 μm cannula (G27 needle) or in the form of a topical/superficial application. To precisely deliver the intended volumes of peptide formulation, we developed a handheld device that can accurately deliver volumes ranging from 10 μL to 1.0 mL (Figure 2A). This handheld device is equipped with interchangeable nozzle adapters, which were specifically designed for the different applications reported here. Further specifications on the device are found in the Supporting Information section of this article (Figures S14–S16, Supporting Information), including details for the engineering of the nozzle adapters (Figures S17–S19, Supporting Information). In <https://figshare.com/s/f195a5a27ccfc9072225>, printable STL files for all components of the device are made available at no cost. Further, in the case of the injectable versions of the materials, to inject our material more easily through a needle, we wanted a lower viscosity along with shear-thinning properties, which are common in large polymer networks like the one our material is composed of. To measure these properties, we performed viscosity measurements. Our lower concentration CM_{ratio} 1.0 formulation had a much lower viscosity at 100 s^{-1} shear rate (3.8 ± 2.4 and 20 ± 9.0 Pa*s, for CM_{ratio} 1.0 and 4.0, respectively), while demonstrating shear thinning properties like other injectable materials such as Viscoat (≈ 4.0 Pa s) and was thus chosen for injection applications.

In the following sections, we present proof of concept experimental data for assessing the feasibility of using our material for skin wound closure, for treating cornea perforations and in situ cornea reshaping, and as an injectable intramyocardial material.

2.2.1. Peptide-Based Materials for Skin Wound Healing

We started by assessing the skin bonding properties of the different formulations by performing *ex vivo* wound closure testing using murine skin (Figure 2B). In terms of the structure, murine skin and human skin are similar. The difference is that murine skin has a thinner dermis and no sweat glands, and wound healing occurs primarily through contraction, whereas human skin wounds close by granulation tissue formation.^[46] The results indicated that only the Pep-5 formulation possessed skin bonding properties comparable to those obtained for BioGlue, a clinically used tissue adhesive comprising 45% bovine serum albumin with 10% glutaraldehyde^[47] whose mechanical properties remain constant within our screened timeframe (Figure 2C). The Pep-5 formulation bonding strength was superior to the rest of the screened peptides except for peptides 19, 20, and 21, which are variants of Pep-5 (Figure S20, Supporting Information). However, the gelation for those peptides was too rapid, making them unpractical for on-the-spot tissue repair application (Figure 1B). Further, our findings indicate that the structural properties and amino acid sequence of Pep-5 are critical for functional tissue bonding, as the effectiveness of these gels is affected by the self-assembly of the peptide chains. Thus, for example, removal of a cysteine from either side of the peptide (Pep-8 and –9) results in a bonding strength of only a few kPa while removing both cysteines (Pep-10) results in no gelation. Disruption of folding with a Gly-Val substitution in the middle of the sequence (Pep-15) results in a significant loss of $\approx 50\%$ in bonding strength. Using a lower CM_{ratio} of Pep-5 (1.0) or diluting the CM_{ratio} (4.0) results in weaker bonding (Figure 2D). Further testing of the CM_{ratio} 4.0 non-diluted formulation indicated that bonding strength gradually increases after application, from ≈ 50 kPa at 30 min to ≈ 100 kPa at 60 min (Figure 2E). While bonding is one of the key parameters, shear adhesion strength is also a useful parameter to evaluate. Note that in lap shear studies, porcine skin is more often used.^[48,49] However, the modulus of porcine skin, murine skin, and human skin are reported as similar.^[50] Adhesivity testing of the Pep-5 CM_{ratio} 4.0 showed that the adhesivity of our peptide-based material is comparable to that of BioGlue (Figure 2F). Young's modulus values for the materials were 82 ± 50 , 61 ± 14 , and 10 ± 3 kPa for CM_{ratio} 1.0, 4.0, and BioGlue, respectively. Representative profiles for the stress versus strain values are provided in Figure S21 (Supporting Information). Having identified Pep-5 as the top peptide candidate, we further assessed the material porosity. An average pore size of ≈ 10 μm was observed after swelling for the Pep-5 materials (Figure S22, Supporting Information). In the next section, we focus on presenting data on the Pep-5 CM_{ratio} 4.0 formulation as a tissue sealant for skin and cornea applications.

The material's potential cytotoxicity was evaluated using *in vitro* tests for assessing the viability of human skin cells. The data indicated no adverse effect on the viability of cells exposed to the peptide-based materials (Figure S23, Supporting Information). We then assessed the wound closure ability of the peptide-based material in a full-thickness murine wound model (Figure 3A). It should be noted that murine skin wound healing occurs primarily through contraction, whereas human skin wounds close by granulation tissue formation. So, while the mouse skin model is useful for initial testing, it is not an ideal representation of

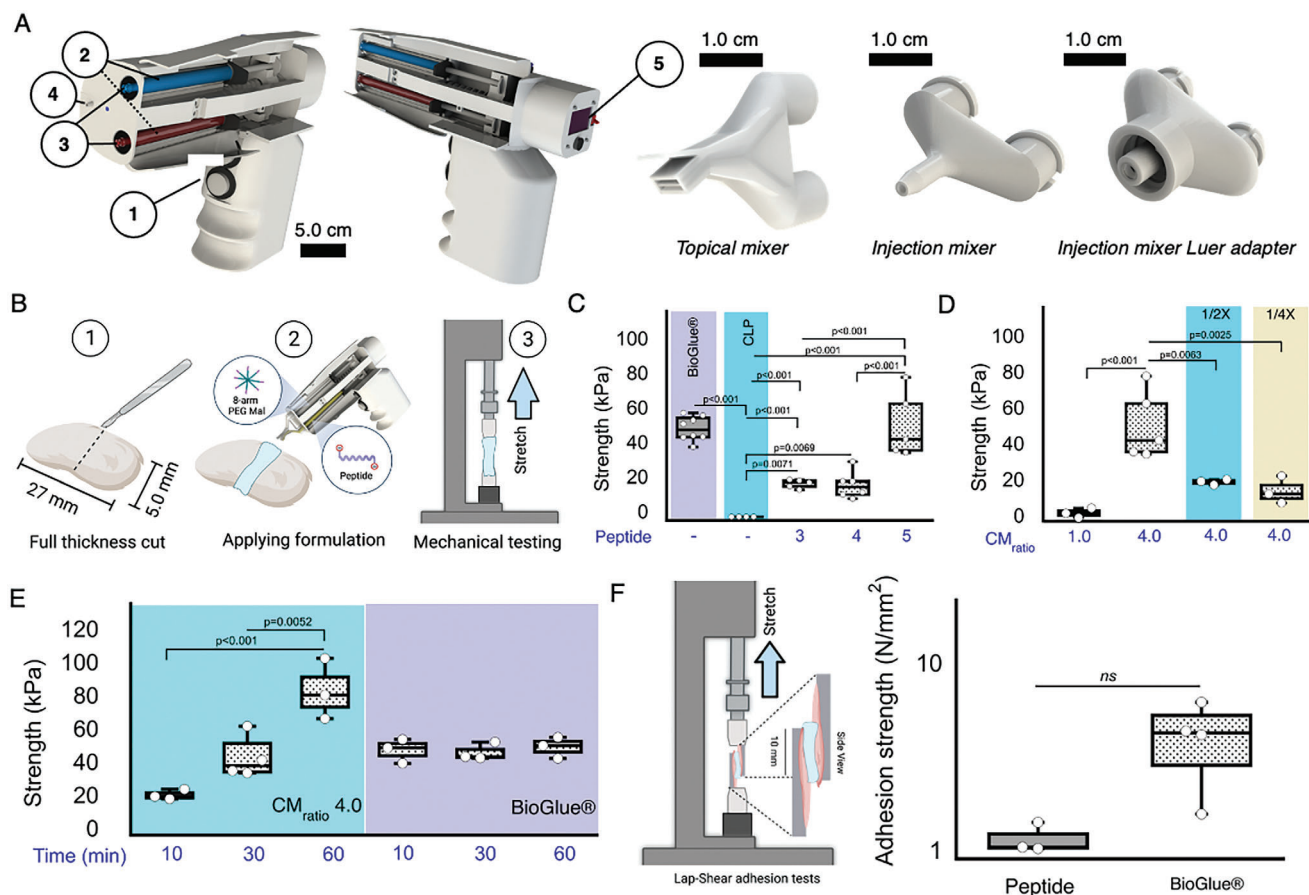


Figure 2. Peptide-based materials can be used to bond tissues better than current commercially available products. A) *Left:* 3D renders for the custom-designed hand-held device for delivering the peptide-based materials designed in this study. The render displays the main features of the device that include: (1) dispensing on/off control, (2) enclosed compartment for placing peptide-cartridges (preloaded syringes), (3) aperture for nozzle adapters, (4) camera port for live monitoring, and (5) digital controller screen for volume and speed settings. *Right:* Three representative nozzles designed for the hand-held device presented herein for topical application (left), cornea sealant delivery (middle), and intratissue injection (right). B) Schematic depiction for the procedure followed to assess skin bonding in a full-thickness incision. Bonded tissue was assessed using uniaxial mechanical stretching tests perpendicular to the wound. Bonding strength was measured an hour after application for Figures 2C, D, and F. C) Mechanical strength (kPa), also known as wound closure strength test (ASTM F2458), measured for murine skin tissue after application of peptide-based formulations CM_{ratio} 4.0 (10 mm min⁻¹ extension) for top peptide-based hydrogels prepared using peptide 3, 4, and 5. Values measured for applications of BioGlue® and the collagen-like peptides (CLP) are also included in the plot ($n = 7-8$). D) Mechanical strength (kPa) for murine skin tissue measured using the 4.0 ratio at two different dilutions (1/2 and 1/4; $n = 3-5$). E) Changes in bond strength as a function of time post-application (10, 30, and 60 min). Samples were incubated at 37°C in 100% humidity ($n = 3-4$). F) *Left:* Illustration for lap-shear tests using porcine skin using a 10 mm min⁻¹ extension. The adhesion surface was fixed at 50 mm². The adhesive (peptide-based formulation or BioGlue®) was applied within the two pieces of skin. *Right:* Adhesion strength values measured for the peptide-based formulation CM_{ratio} 4.0 and BioGlue® ($n = 3-4$, $\approx 50 \mu\text{m}$ thickness for the peptide or BioGlue®). P-values for C, D, and F were calculated using One-Way ANOVA and a post-hoc Holmes correction. P-values for F were calculated using a student t-test (unpaired unequal variance).

human skin, and the use of other models will be needed in future studies to further elaborate the potential of our peptide-based hydrogels for skin repair. The animal model used a 7-day endpoint to evaluate the inflammatory response and tissue remodeling as previously reported.^[51] Pictures of the wounds at 0, 1, 3, and 7 days clearly showed the peptide-based material is cosmetically superior to sutures or BioGlue (Figure 3B). The data presented here corresponds to those wounds that did not dehisce. Note that wound dehiscence after 1 day was observed in $\approx 25\%$ of the animals that received BioGlue and $< 5.0\%$ for animals that received the peptide material. Also, debonding of the peptide adhesives was not observed. Mechanical

testing of wound skin freshly harvested after euthanasia indicated that the peptide-based material is superior to sutures and BioGlue, and comparable to unwounded skin (Figure 3C). Histological analyses of the tissues showed that the peptide-based material presents a more functional wound healing, including increased collagen deposition and reduced epithelial thickness (Figure 3D). Further histological assays carried out to evaluate the number of pro-healing macrophages indicated that the animals treated with the peptide-based material have no difference in the number of CD206+ macrophages compared to the sutures or BioGlue groups (Figure S24, Supporting Information).

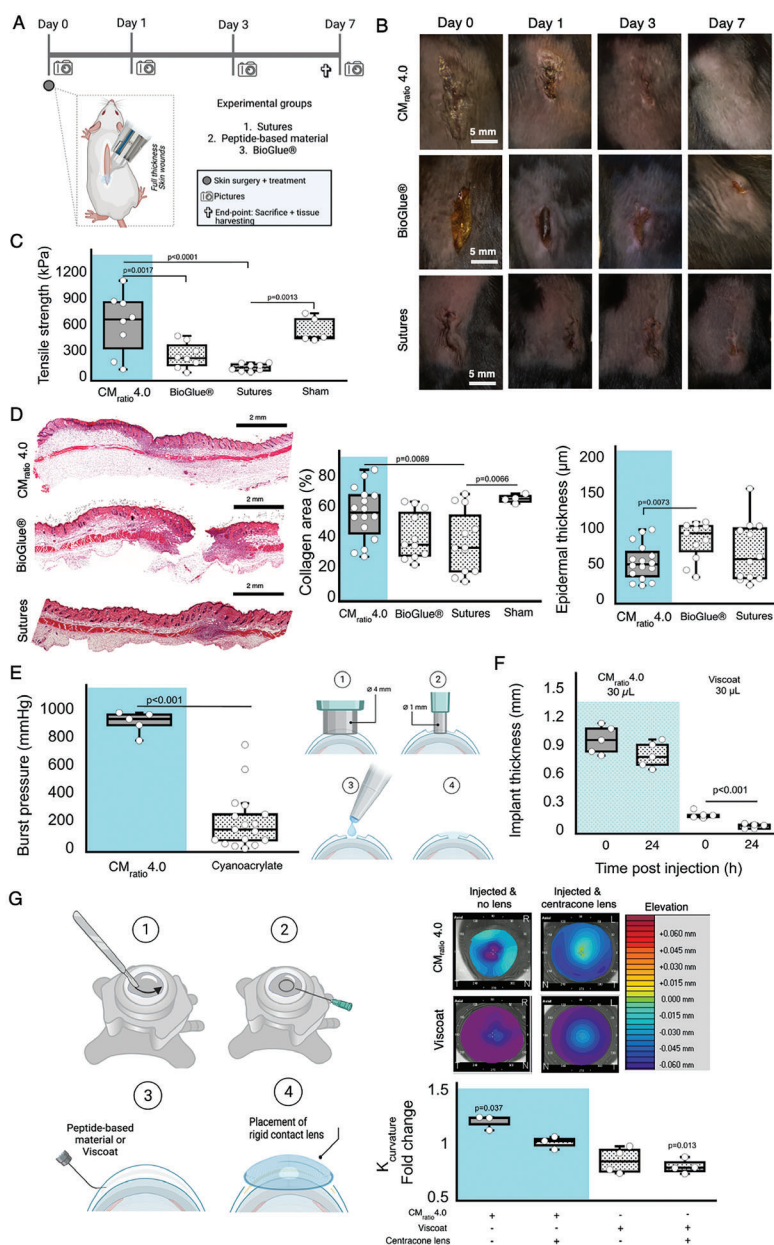


Figure 3. Peptide-based materials as tissue bonding sealants and fillers. A) Schematic of the experimental design used for the *in vivo* testing of the tissue bonding capabilities of the peptide-based materials using C57BL/6 female mice (7–8 weeks). B) Representative images of the full-thickness wounds taken at 0-, 1-, 3-, and 7-days post-treatment for the different experimental groups. Scale bars = 5.0 mm. C) Mechanical strength (kPa) for murine skin tissue measured 7 days post-operation ($n = 5–8$) obtained for the different experimental groups. The Sham group corresponds to animals that underwent the same steps as those that received incisions, but the skin remained intact. D) *Left*: representative histological images of the skin at 7 days for the 3 treatment groups. *Right*: Analysis of the histological sections obtained for the different treatment groups including collagen deposition ($n = 4–16$), and epidermal thickness ($n = 11–16$).^[55–57] E) *Left*: Burst pressure values measured for the peptide-based material CM_{ratio} 4.0 or cyanoacrylate ($n = 5–17$). *Right*: Illustration for the pig cornea perforation *ex vivo* model used in this study. The numbers in the Figure illustrate: (1) initial perforation to create a wound bed, (2) inner full-thickness cornea perforation using a 1 mm biopsy puncher, (3) application of the treatment to seal the hole, and (4) formation of a “corneal” patch. F) Changes in implant thickness were obtained using 30 μL of the CM_{ratio} 4.0 peptide material or Viscoat ($n = 5$). G) *Left*: Illustration of the *ex vivo* pig cornea pocket and cornea reshaping model used in this study. The numbers in the figure illustrate: (1) initial surgical incision to create a wound bed, (2) insertion of needle to open a cavity, (3) injection of the peptide-based material as an intracorneal patch, and (4) positioning of a solid contact lens. *Right top*: Representative corneal topographic axial maps showing surface elevation of corneas injected with either CM_{ratio} 4.0 or Viscoat. The topographic maps are generated for corneas before injection, after injection, and injection in conjunction with insertion of a rigid contact lens (Centracone). The scale on the right shows the height in mm, with warmer colors representing steeper areas and cooler colors marking flatter ones. *Right bottom*: Fold change for K values of curvature (mm) obtained for corneas that have been injected with either CM_{ratio} 4.0 or Viscoat, with the placement of RGP/Centracone rigid contact lenses in conjunction with the peptide-based material ($n = 4$) with volumes $\approx 30 \mu\text{L}$ (compared to empty pocket). For C and D, p values were calculated using One-Way ANOVA and post-hoc Holmes test, while student t-tests were used for E and F (unpaired unequal variance) and G (paired data).

2.2.2. Peptide-Based Materials for Cornea Repair

The bonding capacity of the peptide-based material, which is comparable to that of BioGlue, makes the minimalistic material suitable for soft tissue repair. We further assessed if it could be used for rapid closure of perforated cornea tissues, an application that is amenable due to the transparency of the materials. As an *ex vivo* model, we chose a cornea perforation system, which is readily used to test the suitability of a material for sealing a perforated tissue.^[52] Figure 3E depicts the data and schematic representation for the *ex vivo* model we used. Pig corneas were used as they are physiologically similar to humans.^[53] The data indicated that the burst pressure conferred by treatment with the peptide-based material is higher and more reproducible than cyanoacrylate as a corneal sealant (Figure 3E). While cyanoacrylate remains one of the gold standards for rapid corneal sealing in emergency situations, its observed toxicity toward corneal tissues presents the main drawback for its safe use.^[54] In contrast, the peptide-based material did not exert significant toxicity toward human corneal cells (Figure S25, Supporting Information), which positions this technology ahead in the space of corneal repair. Further, another potential application for the peptide-based material could be as an *in situ* corneal filler. Data indicates that rapid injection of CM_{ratio} 4.0 into the pig cornea renders implants that are considerably thicker and more stable than those produced using Viscoat (Figure 3F). Further, we assessed the ability of the peptide-based material to reshape cornea curvature in an *ex vivo* model. Figure 3G includes a schematic representation for the experiments, showing the creation of an intrastromal pocket in the pig cornea, which can be filled with a viscous material, such as the peptide hydrogel. After injection of the peptide-based material, an increase in cornea curvature was measured compared to the control (Figure 3G). Upon application of the rigid contact lens, a change in the cornea shape is detected for the peptide-based material when compared to the injected cornea and no lens. Curvature changes for corneas treated with Viscoat and lens shows that injection of Viscoat does not achieve a significant change in curvature when compared to the pocket alone. In fact, there is an overall decline in cornea curvature for the corneas that received the centracone lens and Viscoat. Refractive index measurements for pig corneas containing the peptide-based material indicate no significant differences in refractive index [1.36 ± 0.011 and 1.35 ± 0.014 ($n = 16$, $p = 0.43$) for cornea and cornea + peptide, respectively]. While preliminary, this data suggests the peptide-based material developed in this work offers a cost-effective alternative to cyanoacrylate, including the possibility to *in situ* reshape the cornea.

2.2.3. Peptide-Based Materials for Treating the Infarcted Heart

The data presented in Figures 2 and 3 indicate that the CM_{ratio} 4.0 hydrogel has high potential as a tissue adhesive, sealant, and filler material; however, for intramyocardial injection, such materials are too viscous to be delivered using multiple injections through G27 diameter needles. Thus, for intramyocardial applications, we tested the suitability of the CM_{ratio} 1.0 material, which is approximately an order of magnitude less viscous at high shear rates (20, 3.8, and ≈ 4.0 Pa s for CM_{ratio} 4.0 and 1.0 and Viscoat at

100 s^{-1}). For *in vivo* testing, we used a clinically relevant murine myocardial infarction (MI) model that recapitulates patients who have not responded to revascularization therapeutics or who have delayed seeking treatment.^[58] The model involves the permanent ligation of the artery descending blood flow supply to induce MI, followed by treatment delivery at 7 days post-MI (Figure 4A). There were no toxicity concerns since the CM_{ratio} 1.0 material did not affect human cardiac endothelial cell viability *in vitro*. The percentage of viable cells was not statistically different for the peptide-based material compared to a collagen-based hydrogel after 2 days of culture (Figure 4B). Assessment of the left ventricular ejection fraction 4 weeks after treatment delivery showed that the intramyocardial injection of the CM_{ratio} 1.0 material preserved cardiac function of the MI heart (i.e., no fold-change versus baseline, $p > 0.05$) compared to the control group (Figure 4C). However, no differences in scar size (Figure 4D) or the number of pro-healing macrophages (Figure 4E) were observed. Use of fluorescent labeling to track the CM_{ratio} 1.0 material *in vivo*, showed that it could still be visualized in the cardiac muscle for up to 7 days after injection (Figure 4F). This finding presents an interesting opportunity for use of the CM_{ratio} 1.0 material for the *in situ* delivery of therapeutic agents, such as small molecules, biopolymers, or extracellular vesicles that typically have low retention rates when delivered to the myocardium.

3. Discussion

The technological development of biomaterials remains costly and time consuming.^[59] Further, material testing often necessitates the use of relatively large sample volumes, which hinders biomaterial discoveries when peptide libraries are being used. Here, we used a strategy that is time and cost effective, by reducing the number of potential peptide candidates and formulations by one order of magnitude compared to traditional screening methodologies that need larger volumes and exhaustive testing times. The screening approach used small sample volumes ($\approx 50 \mu\text{L}$) of the peptide candidates, which considerably reduces screening costs and time burden of their synthesis, critical when dealing with peptide synthesis. We limited the number of amino acids in each peptide as much as possible as each extra residue increases synthetic cost and difficulty; thus, the ideal candidate would possess the desired properties while minimizing residue number. The choice of screening tests used in the strategy combined with the facile material assembly process enabled by our selection of chemistries allowed us to rapidly screen different formulations.

Our peptide-based material utilizes the structural backbone of the peptide as both the crosslinker and a structural component. This approach uses a synergistic dual mechanism, inspired by how structural collagen organizes in natural tissue, where orthogonal chemistry and supramolecular assembly are key. Peptide supramolecular assembly is usually thought of in terms of alpha helix and beta sheet folding, but we show that collagen triple helical folding can be utilized to create and reinforce materials. Using a library of peptide structures and a rapid screening procedure for gelation, we identified some key structural components needed to render peptide structures that can *in situ* assemble to a PEG backbone. Further, the resulting hybrid peptide-copolymer displayed desirable and tunable physical

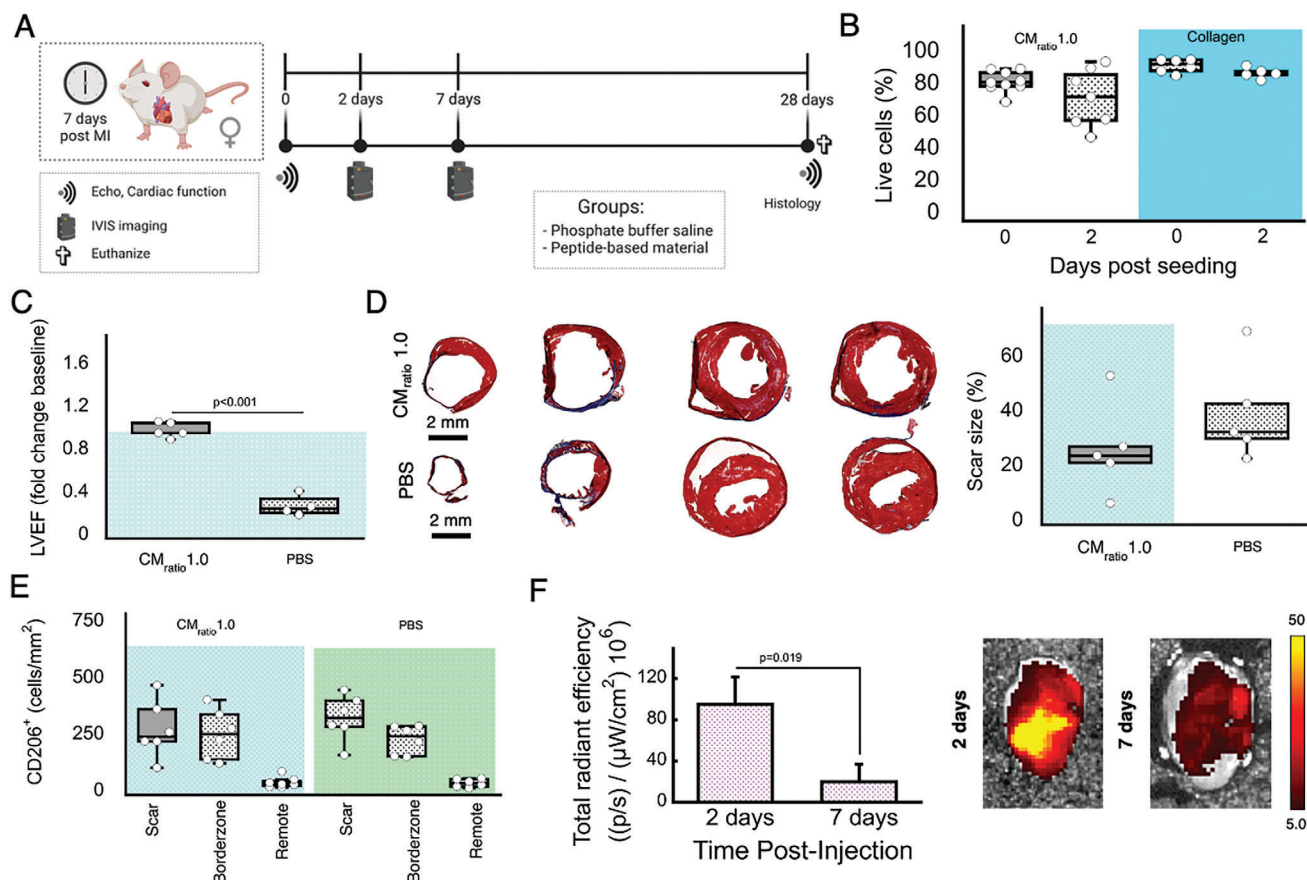


Figure 4. Peptide-based materials can be safely injected intramyocardially and remain within the cardiac muscle. A) Schematic of the experimental design for in vivo testing of the intramyocardial injection application of the peptide-based materials. Experiments were carried out using C57BL/6 female mice (7–8 weeks). B) Percentage of live human cardiac endothelial cells measured at 0 and 2 days after seeding on the CM_{ratio} 1.0 material or collagen-based hydrogel ($n = 5–9$). C) Left ventricular ejection fraction (LVEF) fold change relative to baseline measured 28 days after treatment with CM_{ratio} 1.0 material or PBS ($n = 4–5$). D) *Left*: Representative Masson trichrome staining images for hearts treated with CM_{ratio} 1.0 material or PBS. *Right*: Analysis of the scar size for the two treatment groups ($n = 5$). E) Number of CD206⁺ cells counted in myocardial tissue sections within the scar, border zone, and remote areas ($n = 6$). F) *Left*: Quantification for *ex vivo* fluorescence imaging ($\lambda_{excitation} = 570$ nm; $\lambda_{emission} = 640$ nm) of hearts injected with the Alexa-Fluor@594-labelled CM_{ratio} 1.0 material at different days post-injection. *Right*: Representative IVIS images of the MI hearts harvested after 2- or 7-days post-injection ($n = 3$). *P* values were calculated using student t-test (unpaired data & unequal variance).

properties that can be adjusted simply by utilizing different peptide:PEG ratios, thus making them amenable for use in different tissues. A pore size of 10 μ m, such as observed for our peptide-based materials, is suitable to allow for cell invasion and integration of the hydrogel with the host tissue.^[58] Also, the material preparation is straightforward requiring only reagent solvation in minutes, without the need for external crosslinkers, special solvents, or purification and is sufficiently robust to be performed in situ when compared to other peptide-based biomaterials.^[22,60] For future clinical use, similar to other clinically used materials such as BioGlue, our technology will be delivered using a two barrel-syringe system that will allow a single hand operation.

The peptide-based materials displayed adhesive properties comparable to those of BioGlue, which is remarkable when considering no specific adhesive moieties were added to the peptide sequence. Some key advantages of the material include simple, rapid in situ gelation, tunable hydrogel strength and adhesiveness, and a fully defined chemical composition. A fully defined

composition and fully synthetic nature of the peptides compared to extracted animal gelatin-based materials provides greater safety and consistency for clinical use. Further, the synthetic nature of the peptides will allow for additional post-refinement of the matrix composition such as adding motifs that recognize specific cellular proteins for promoting specific cell interaction and function. The tunable gelation of the material allows for its use as a topically applied material or in the form of an injectable material by simply using a syringe-mixing system. Typically, peptide gels that form solely from supramolecular assembly are weak and applied only as a topical dressing.^[61] Instead, our materials can achieve a wound closure strength of up to ≈ 100 kPa, whereas a pure peptide gel such as a recently reported tryptophan zipper system had a yield strength of 0.075 kPa.^[62] Another LDLK12 peptide gel reported a failure stress of 0.019 kPa that could be increased to 0.035 kPa with EDC/NHS crosslinking.^[63] Compared to other PEG-peptide systems,^[64] our peptide-based material renders stronger gels more quickly at physiological pH. Peptide hydrogels are often used as carriers for drug delivery,^[65] which is

another promising application for which our materials would be highly suited.

Biomedical systems should be cost-effective and practical to find adaptation. As the number of peptide drugs in clinical trials continues to increase^[66] and novel peptide drugs such as Semaglutide^[67] receive media attention, peptide synthesis is becoming a scalable industrial process that can produce kilograms^[68] or even tons^[69] of finished product. Peptides of ≈ 30 amino acid residues, such as the 31 residue Semaglutide, are considered relatively short and can readily be scaled for industrial production.^[69,70] While not strictly scientific, costs of production should also be considered when thinking of clinical translation and technology adoption. Thus, the cost to access peptides is reasonable for biomedical standards, with retail Semaglutide selling for ≈ 150 USD g^{-1} in the least expensive markets.^[71] Therefore, our peptide-based materials, which consist of short peptide sequences and are composed of only two components that can be stored as solids, offer a cost-effective approach for generating peptide-based therapeutics for tissue and organ repair.

Due to their rapid gelation and adhesivity, our peptide hydrogels could be applied to the cornea surface to seal perforation defects or injected into the corneal stroma to alter its shape. Furthermore, treating skin wounds with our peptide hydrogels resulted in visibly accelerated healing along with histological markers of improved repair including reduced epithelial thickness and increased collagen content. While our data illustrated low macrophage polarization, it has been described that macrophage expression varies across time during the process of wound healing as initially M1 macrophages are seen, then replaced with M2 macrophages, and lastly both are gone from the wound as it heals and matures.^[72] Further, a moist wound environment, such as one provided by hydrogels, is beneficial toward wound healing^[73,74] and thus our material is suitable as a wound sealant.

The peptide-based material can also be injected into the ischemic area of the heart after mixing two components, rapidly forming a gel. In a mouse model of MI, injecting it in situ for 28 days-maintained heart function in contrast to the loss of function observed for the control group. Peptides and other biological molecules can be rapidly degraded in living organisms. Imaging experiments show that the hydrogel remained in the myocardium for at least seven days, offering the potential for in situ drug or cell delivery. A previously reported peptide-based injectable material for treating heart tissue post-MI consisted of an elastin-mimetic peptide hydrogel with great mechanical strength under the action of upregulated trans-glutaminase.^[75] However, a limitation is the complex and time-consuming preparation methods that are needed;^[76] in contrast, our peptide-based material is prepared rapidly, which is more convenient and simpler to operate with, thus making it more suitable to clinical application. Further, our findings open new avenues for enabling modifications of the materials using the peptide structures and orthogonal click chemistry, such as chemical functionalization of the PEG core,^[77,78] which would allow for the prolonged delivery of small drugs and molecules.

While the peptide-based technology presents several advantages, potential shortcomings include the irreversible nature of the strong chemical bonding. Also, as the reaction begins immediately after mixing, control of the final shape can be less precise compared to remotely activated materials.^[79] Further, compared

to some other peptide hydrogels,^[80–82] our gels cannot self-heal. However, the tunable nature of our peptide-based hydrogel synthesis approach is amenable to modification and/or functionalization that could confer those materials with such properties, which could be tested in the future.

In summary, our cumulative data illustrate that engineering the chemical structure of collagen-like peptides allows for the development of functional crosslinking backbones suitable for the formation of hydrogels. The data also indicates that these peptides must contain at least two cysteine thiol-reactive groups for Michael addition click chemistry with adequate steric spacing, and that the supramolecular assembly of these peptides contributes to hydrogel strength. This unique combination of engineered click-self assembling peptides allows for the rapid in situ production of adhesive, multifunctional, and tunable hydrogels. These injectable materials were assessed and shown to be effective for therapy in three separate soft tissues including the skin, cornea, and heart. The simple yet robust chemistry, combined with the peptide engineering used to produce these gels leaves ample room for future biofunctionalization and/or loading of drugs, extracellular vesicles, or other payloads.

4. Experimental Section

Peptide Synthesis: Fmoc protected amino acids and low-loading Wang resin were purchased from CEM. All peptides were synthesized using microwave assisted Fmoc solid phase peptide synthesis (SPPS)^[83] in a Liberty Blue automated system. Briefly, the required amount of resin was swelled in DMF for 5 min. Next, Fmoc deprotection was carried out with 20% piperidine at 90 °C for 60s. Standard coupling cycles using DIC/Oxyma Pure were run at 90 °C for 240s in each amino acid. For difficult couplings, the temperature was increased to 100 °C and additional reagent equivalents/double couplings were used along with an increased reaction time and addition of urea as a chaotropic agent. Peptides were cleaved from the resin and deprotected with TFA/TIS/EDT/H₂O (92.5/2.5/2.5/2.5%v/v) at 42 °C for 30 min, and then precipitated in -20 °C diethyl ether. Peptide crude products were then dried under vacuum overnight and purified by preparative RP-HPLC in an Agilent 1260 Infinity II system with a 30 \times 100 mm Agilent C18 column at 50 mL min^{-1} . Peptide purity and identity were confirmed via analytical LC-UV/MS in an Agilent 1260 Infinity II system using a 4.6 \times 100 mm Agilent C18 column. A gradient of 0% to 40% phase B over 20 minutes was utilized with phase A consisting of water/acetonitrile 5%/formic acid 0.1%/TFA 0.01% and phase B acetonitrile/water 2%/formic acid 0.1%/TFA 0.01% at a flow rate of 1.5 mL min^{-1} . A purity of >95% was determined through HPLC peak analysis. Table S1 (Supporting Information) contains a summary of the detailed mass spectrometry data for the peptides alongside each individual spectrum. Table S1 (Supporting Information) includes a summary for peptide crude purity and Figure S26 (Supporting Information) displays representative HPLC profiles for the peptides.

Peptide purity and identity were confirmed via LC-UV/MS in an Agilent 1260 Infinity II system using a 4.6 \times 100 mm Agilent C18 column. A gradient of 0% to 40% phase B over 20 min was utilized with phase A consisting of water/acetonitrile 5%/formic acid 0.1%/TFA 0.01% and phase B acetonitrile/water 2%/formic acid 0.1%/TFA 0.01% at a flow rate of 1.5 mL min^{-1} . Specific details for the peptide synthesis including cycle time/duration from the CEM device are available directly from the authors. Additionally, the authors are willing to provide small samples of the peptides for those researchers willing to test the peptides herein reported.

Circular Dichroism: Circular dichroism (CD) spectra were collected on a JASCO J-810 CD spectrometer with a bandwidth of 1.0 nm in the ultraviolet (UV) region (190–260 nm) using a 0.5 mm quartz cuvette, at 20 °C using a MPTC-490S accessory. To measure R_{pn} and T_m , all samples were

dissolved at a concentration of 200 μM using phosphate buffer 1 mM (pH 7.4). Then, different dilutions were prepared to obtain 6.25, 12.5, 25, 50, 100, and 200 μM concentrations of each sample to measure folding at different concentrations. The spectra were obtained with solvent background subtraction and were collected with 10 scans.

Infrared Spectroscopy: Fourier-transform infrared (FTIR) spectra were recorded using a Nicolet iS5 FTIR with an Attenuated Total Reflectance (ATR) iD7 accessory and with a diamond crystal. All spectra were taken at 4 cm^{-1} of resolution, and 64 scans in the 4000–500 cm^{-1} range at room temperature. Before measurements, the prepared peptides and hydrogels were freeze-dried. The FTIR spectra of the Amide I region (1750–1550 cm^{-1}) were then fitted by multiple Gaussian peaks, see further details in Supporting Information and Figures S10–S13 (Supporting Information).

Computer Modelling: The homology models for the entire set of peptides (see Figure S5, Supporting Information) were obtained using the ColabFold tool.^[84] This tool is a free and accessible platform for protein folding and provides accelerated predictions of protein structures and complexes using AlphaFold2. The 3D structure predictions from its sequences are achieved by using multiple sequence alignments (MSA) of related proteins as input for end-to-end training.^[85] To build the diverse MSAs, a large collection of protein sequences from databases is searched using both HMMer^[86] and HHblits^[87] methods, both of which use profile hidden Markov Models.

As a first step in the modeling protocol, a single-stranded structure is generated for the entire set of peptides. These modeled strands were then replicated to generate the triple helix-like structure, using collagen type 1 as a reference.^[88] Each peptide was then solvated with 15 Å in each of the 3 cartesian coordinates, using the TIP3P water model, resulting in water boxes of varying sizes depending on the peptide's dimensions. Sodium ions (Na^+) and chloride ions (Cl^-) were added to neutralize each system.

Molecular Dynamics: The NAMD software was utilized to conduct molecular dynamics simulations employing the CHARMM36 force field.^[89] Integration of the equations of motion was carried out with a time step of 4 fs.^[90] Periodic boundary conditions were applied in all three dimensions. An NPT ensemble was employed to maintain constant temperature (300 K) using Langevin dynamics and constant pressure (1.0 atm) using the Nosé-Hoover-Langevin piston.^[91] The peptide backbone was harmonically restrained using the Colvars module^[92] to restrict vertical movements. Additionally, center of mass colvars was applied to avoid issues related to periodic boundary conditions. All systems were minimized for 20,000 steps, followed by five equilibration simulations. In these simulations, initial position restraints were subsequently reduced every 5 ns, to finally perform unrestrained equilibration simulation for 500 ns.

Simulation Analysis: Each peptide model was aligned based on the CA atoms of the backbone to conduct distance measurements along the z-axis, only on the last 200 ns. Our focus was on the Cys residues of each peptide, specifically the sulfur atom, and for those sequences without cysteine, the analysis was conducted at the CA atom of the amino acid in the third position, which was the most common position of cysteine in each of the sequences. To assess the degree of openness at each terminal end of every peptide, the distance from the sulfur atom to the projection onto the z-axis passing through the center of the three strands forming the peptide was measured. Consequently, the distance from each sulfur atom in every chain was measured for each peptide, both at the upper and lower ends, along the last 200 ns of simulation. Additionally, to capture the positional fluctuation of each residue, the Root Mean Square Fluctuation (RMSF) analysis was performed for each peptide, with the initial model serving as a reference point. Similarly, the Root Mean Square Deviation (RMSD) was analyzed, indicating the average change in peptide structure during molecular dynamics relative to the initial simulation point; for both analyses, the last 200 ns of the simulation were also considered (see Figure S6, Supporting Information).

Hydrogel Preparation & Peptide Selection: Hydrogels were prepared from three components: peptide, 8-Arm PEG-Maleimide MW 40K, a long bearing chain that is easy to form a network (Creative PEGworks, USA), and a buffer solvent. Reagents were freshly dissolved in buffer before use and kept on ice until application. Three different formulations of peptide

to PEG-Mal were used: CM_{ratio} 1.0, 3.0, and 4.0. Solutions were loaded into syringes and administered to the target site for in situ gelation via our custom applicators. Peptide concentrations ranged from 3.5 to 16 mM. PEG concentrations were kept at $\approx 4.0 \pm 0.5$ mM in all cases. Reagents were freshly dissolved in buffer and kept on ice until use. All hydrogels were prepared with freshly made solutions. Peptide selection included peptides that gel within 15s and 120s, with light transmittance $>85\%$, and a refractive index of <1.38 . For preparing the materials, the components were weighed in a 1.5 ml Eppendorf tube and then ice-cold solvent added. Mixing was done by 30s vortex followed by 5 min of centrifugation (10 000 rpm). Solutions were then transferred into two syringes that were capped by our custom nozzles and stored in ice until use. After incisional wounds were made, the ice-cold material solution was immediately applied to the wound and the mixing of the two component solutions at murine body temperature resulted in rapid in situ gelation. There is a brief time window of ≈ 30 –60s before the material begins to solidify where it can be spread over the wound and molded into a desired shape.

Gelation Time Testing: Gelation time was calculated using fluid mechanics on an inclined plane.^[93–95] The methodology present here was adapted from international standards used to measure oil-like products and thickening agents on inclined planes for the purpose of finding the specific point where the liquid loses its flow characteristics. As fluid viscosity increases, the velocity of the flow reduces until it becomes static, indicating that the substance has transitioned from liquid to solid. The gelation time was measured using a 22.5° inclined plane with 50 μL samples placed on the glass inclined plane. Sliding time and distance recorded for up to 3 min (see Figure S26, Supporting Information) using a mounted 1080p HD iPhone 6 camera (software iOS 13.3) and the individual gel movement was tracked via iMovie (10.4). Average times for all samples ($n = 5$) were reported. Printable STL file used in the screening are available in <https://figshare.com/s/f195a5a27ccfc9072225>. Peptides 1 to 21 and CLP were evaluated at CM_{ratio} of 1.0, 3.0, and 4.0. All experiments were carried out in a double-blind fashion. The operator and data analyzer had no information on the nature of the sample being experimented or processed.

Transmittance: The absorbance and transmittance of the hydrogels were evaluated using a SpectraMax M2/M2e microplate reader (Molecular Devices, USA). The hydrogels (20 μL) were placed on a 96-well plate containing 150 μL of PBS, the absorbance was measured at a wavelength of 550 nm. As a control, the absorbance of wells containing 150 μL of PBS was measured. The method for calculating percent transmittance was: % Transmittance = $10^{(2 - \text{absorbance})}$. The peptides studied were 1 to 21, as well as CLP at the $\text{CM}_{\text{ratios}}$ of 1.0, 3.0, and 4.0.

Refractive Index Measurement: The refractive index was measured with an Abbat 300 refractometer (Anton Paar, Canada) at a temperature of 37 °C. The hydrogel samples were made on a glass slide and transferred into the refractometer sensor where the nD index was recorded and reported.

Collagenase and Water Content: The stability of the hydrogels was assessed by soaking them in collagenase from Clostridium histolyticum (Sigma-Aldrich, USA) at 5 Unit mL^{-1} in 0.1 M Tris-HCL Buffer containing 5 mM CaCl_2 and measuring their loss of mass over time.^[58] Percentage of residual weight was calculated as: residual mass (%) = $W_{\text{(total)}}/W_{\text{(initial)}}$. The calculation of water content was evaluated by comparing the mass of the casted hydrogel against the lyophilized mass.

Lap-Shear Test: A modified ASTM F2255-05 standard was utilized to conduct this test. This was performed at a pace of 10 mm min^{-1} on an Instron 3342 universal testing machine (Instron, USA) and analyzed using INSTRON Series IX/S (Instron, USA) software. The samples consisted of applying the hydrogel to a 0.5 cm^2 section of pig skin. The force and strain of each sample were recorded as it was pulled to failure.

Viscosity: The viscosity of each formulation was measured using a Brookfield viscometer with an RCT-25-1 spindle. The micrometer ring of the rheometer was first set to zero and then the measuring head was lowered to the zero position. The spindle was tightened and then the micrometer was set to the measuring point (M) allowing for 50 μm of space between the spindle and the bottom plate. Equal volumes of peptide-5 solution and 8-arm PEG maleimide (100 μL total) were mixed and added to the center of the plate. The spindle was fully lowered, and excess sample

was removed. The viscosity was measured between 0–200 s⁻¹ shear rate at 25 °C using Rheo3000 v2 software.

Denaturation Temperature: The thermal properties of the gel were measured via differential scanning calorimetry analysis with a DSC-Q200 (TA instruments, USA). 8 – 10 mg of sample of the various CM_{ratio} were evaluated. The samples were then equilibrated at 20 °C, and then ramped up at 20 °C min⁻¹ to 100 °C, and the total heat flow was recorded. The calibration standard used was Indium.

Material Porosity: Pore size was measured using a standard cryo-SEM protocol previously established.^[58] Briefly, samples were freshly prepared and flash-frozen with liquid nitrogen before being loaded into a Tescan Vega-III XMU (20 kV) under ≈35 Pa pressure with a –50 °C cryostage. SEM images of hydrogels were captured at different magnifications. This method of rapid freezing and measurement helps to preserve the material's structure and pore size before processing.^[96] Hydrogel pore diameter was calculated from the average pore area observed in different regions of the gel using Fiji software.

Wound Closure and Mechanical Strength: A modified ASTM F2458-05 test measured tissue adhesive and sealant wound closure strength.^[97] All animal care and procedures were performed in strict compliance with protocols approved by the Institutional Animal Care and Use Committee (IACUC) at the University of Ottawa Heart Institute. Skin samples were obtained from a cohort of male and female C57BL/6 mice (Charles Rivers Laboratories, Canada). The mouse skin was partitioned into strips of 30 ± 5 mm length, 5 ± 0.5 mm width, and 0.7 ± 0.2 mm thickness. A surgical blade was then used to completely sever the samples at mid-length and simulate a wound. The simulated wound was treated with 30 µL of hydrogel sample to bond the severed skin pieces back together. A few drops of PBS were applied to the ends of the skin strips every 5 min until testing to prevent the mouse skin from drying out. The hydrogel-bonded mouse skin was clamped on an Instron 3342 universal testing machine (Instron, USA) at a 5 mm distance from the simulated wound. The Instron transducer sensor Model 2519 – 101 (Instron, USA) was used to record the formulation's resistance force during the tensile test at a crosshead speed of 5 mm min⁻¹ until material failure. For the control group, the same clamping procedure was used but with an uncut skin sample. Young's modulus and strain % were obtained from the stress-strain graphs. Young's modulus calculations were carried by Instron Series IX/s advanced material tester – version 8.30.

Design and 3D Printing of the Hand-Held Device and Nozzles: All 3D printed components were designed using Solidworks (Dassault Systèmes) and printed on a Form 3B Stereolithography 3D printer (Formlabs). The structural components for the handheld device were printed using Black Resin V4 (RS-F2-GPBK-04) while the mechanical components were printed using Durable Resin V1 (RS-F2-DUCL-02). For the nozzles, the topical mixer was printed using Flexible 80A Resin V1 (RS-F2-FL80-01) while both injection mixers were printed using Clear Resin V4 (RS-F2-GPCL-04). All components for the hand-held device were printed at a resolution of 100 µm while the nozzles were printed at a resolution of 50 µm with automatically generated supports then washed using isopropanol and cured with a combination of UV light and heat treatment. For further details and assembly instructions, refer to the Supporting Information (Figures S10–S15, Supporting Information) and information for printing and assembling. In <https://figshare.com/s/f195a5a27ccfc9072225> printable STL files are made available at no cost.

Skin Incision Sealing Model: C57BL6 female mice (12–14 weeks, weighing ≈22–25 g; Charles River Laboratories) were housed in groups of five until surgery. All animal care and procedures were approved by the University of Ottawa Animal Care Committee and performed in accordance with the National Institute of Health Guide for the Care and Use of Laboratory Animals. Before surgery, mice were given an epidural injection of buprenorphine and put under using general anesthesia (2.5% isoflurane). Dorsal hair was shaved, and the skin was prepped using ethanol swabs. Then, 1-cm full-thickness incisions were made on the back of each mouse using sterile scalpel blades (#15; Integra Miltex).^[98] For suture-closed incisions, four evenly spaced simple interrupted knots were used to close a 1-cm incision using 7-0 nylon suture (#SN5699G; Medtronic; Monosof Black 18" P-13 cutting). For the BioGlue control, 48 µL of bovine serum

albumin (BSA) and 12 µL of glutaraldehyde were topically applied to the incision site as specified in the manual. For the peptide/PEG-maleimide formulation, 30 µL peptide-5 and 30 µL of PEG-maleimide were mixed and topically applied to the incision site using a custom-made nozzle tip (CM_{ratio} 4.0). The mice were allowed to recover on heating pads until mobile and were housed individually. Incisions were assessed on days 1, 3, and 7 post-surgeries for any signs of infection, suture removal, or bleeding, and mice with any of these conditions were removed from the study. After harvesting of the skin, strips of 30 ± 5 mm length, 5 ± 0.5 mm width, and 0.7 ± 0.2 mm thickness were used for mechanical testing.

Histology: Skin tissue from the wound site was fixed in 4% paraformaldehyde for 72 h. Then, skin samples were washed and embedded in paraffin. Hematoxylin and eosin (H&E) staining was done according to the standard protocol provided in a Leica Autostainer XL (Leica Biosystems, Buffalo Grove, IL). Skin epidermal thickness was measured at six different points along the wound site using Fiji and the average thickness was calculated for each mouse wound.^[56] Masson's trichrome stains were done manually using a standard protocol with the Trichrome stain kit (Sigma-Aldrich, St. Louis, MO). To determine the area of blue stained collagen in Masson Trichrome images, a 400 µm x 400 µm region was selected inside the wound region using Fiji. Then, the collagen area for each skin section was calculated by taking the blue stained area and dividing it by the total selected area.^[99] For immunohistochemistry, tissue sections were deparaffinized and washed with PBS and citric acid. Sections were blocked with goat serum and incubated at 4.0 °C with the specific primary antibody: Ab64693 (1:200) for CD206. Further labeling was performed with specific secondary antibodies: AF488 anti-rabbit secondary (ThermoFisher, A-11008 at 1:500 dilution). The fixed cell nuclei were subsequently stained with DAPI. Images of the samples were obtained under a microscope, with each section taken at 10x and 40x magnification, respectively.

Ex Vivo Pig Cornea Model Mounting: Pig eyes were obtained from certified local farms. Freshly harvested eyes were transported in an ice bucket and processed the same day. Eyes were disinfected in Iodine-PVP (10%) for 2 min and then transferred to sterile 0.1% sodium thiosulphate solution for 1 min before immersion in sterile saline solution for 2 min. Using a scalpel blade, a small (5–8 mm) incision was made at the equatorial and carefully extended by 360° around the entire eyeball while avoiding perforation of the underlying choroid layer. Once the cut was made, the ciliary body-choroid was pulled downwards using forceps to avoid touching the corneal scleral disk. The corneal scleral disk was held in place using a pair of tweezers and the retina was peeled off the inside of the corneal scleral disk using another pair of tweezers. Then, the corneal scleral was rinsed with PBS and placed in DMEM media containing 10% FBS, 1% Gentamycin antibiotics (ANTI-ANTI), and HEPES 15 mM. The corneal scleral disk was placed on the base of the perfusion chamber developed in our lab (size 18 mm, 45° angle).^[100] The chamber was twisted clockwise while maintaining downwards pressure on the chamber base to prevent sliding of the cornea and to tightly seal it in place. The chamber was then filled with DMEM media with 5% dextran using two syringes attached to two irrigation ports that were then attached to maintain an intracorneal pressure within the physiological range.

Injection of Material into Pig Cornea: Following the dissection and mounting of the cornea on the *ex vivo* perfusion chamber, a 6 mm biopsy punch marked with hydrophobic pen ink was used to gently mark the central corneal surface (apex). A 2 mm incision was then made at the edge of this mark to initiate the dissection of an intrastromal tunnel, which was carefully enlarged using a crescent knife to create an intrastromal pocket under the marked corneal surface. For intrastromal injections, each cornea was slightly deflated and 30 µL of the peptide-based material or Viscoat injected into the stromal pockets. Optical coherence tomography (OCT) imaging of injected corneas at 3 timepoints (before gel injection, after gel injection, and at 24 h) was done to assess the ability of the gel to remain constant in the corneal stroma. This was done by measuring the gel thickness in Fiji.

For the cornea reshaping experiments, corneal topographic images were taken using the CT-1000 optical coherence topographer and used to measure the change in corneal curvature before and after the injection of

the peptide-based material or Viscoat. Measurements of corneal curvature were taken from two average K values of steepest meridian and the one perpendicular to it. Images were taken of the natural eye curvature before injection, with a pocket, after the injection, and of the injection with a rigid contact lens (Centracone). Intraocular pressure was held at a maximum across all images and the natural lubrication of the eyes was mimicked with saline and glycerol.

Burst Pressure Testing of Treated Pig Corneas: The same procedure to dissect and mount the pig corneas described above was followed. A perforation was created using a 4 mm biopsy punch at the corneal apex going halfway through the cornea. Following this, a 2 mm biopsy punch was inserted in the middle of the 4 mm perforation to fully penetrate the cornea. Treatment was applied to fill the perforation and the Luer locks of the cornea chamber system were sealed. The flow rate on the syringe pump was set to a steady rate of 18 mL h^{-1} , and the pressure was monitored until the pressure peaked due to the cornea bursting at the sealed perforation site. Windaq data acquisition software was used to monitor the pressure.

In Vitro Human Cardiac Endothelial Cell Culture and Viability Assay: HCECs were cultured in tissue culture plates for 24 h and maintained in HCEC media (Sigma, C22022). The injectable PEG-Pep-5 hydrogel $\text{CM}_{\text{ratio}} 1.0$ formulation was pre-cast in two sterilized glass slides in a humidity box and in a 4°C for 24 h. HCECs (1×10^4 cells per well) were seeded on top of PEG-Pep-5 hydrogel pieces after washing with PBS in a 96-well plate. After 24 h, HCECs were stained using a Calcein-AM and Ethidium Homodimer-1 (CaAM/EthD-1) viability kit (ThermoFisher Scientific, Cat#L3224) according to the manufacturer's instructions. Stained cells were imaged by fluorescence microscopy, and nine random images were taken for each experimental group. Total cell numbers were calculated using ImageJ software (NIH, USA). Each condition was performed in triplicate.

Myocardial Infarction Model and Intramyocardial Injection: All animal care and procedures were approved by the University of Ottawa Animal Care Committee and performed in accordance with the National Institute of Health Guide for the Care and Use of Laboratory Animals. MI was induced in 8-week-old C57BL/6 female mice (Charles River) and treatment delivery was performed using a previously established intramyocardial injection protocol.^[58] Briefly, mice were anesthetized (2.5% isoflurane), intubated, and the heart was exposed via a fourth intercostal thoracotomy. The left anterior descending coronary artery was then ligated just below its emergence from the left atrium. At 1-week post-MI (baseline), mice were randomly assigned to receive one of 2 treatments: (1) PBS (control) and (2) Pep-5-PEG $\text{CM}_{\text{ratio}} 1.0$. The treatment was administered in five equivalent intramyocardial injections ($10 \mu\text{L}$ each site, $50 \mu\text{L}$ total) through a G27 needle using a minimally invasive echocardiography-guided closed-chest procedure. Mice were euthanized by terminal anesthesia at 4 weeks post-treatment and hearts were collected for histological analysis.

Echocardiography and Strain Analysis: Transthoracic echocardiography was performed on parasternal long-axis views using a Vevo3100 system in B mode with a MX400 series real-time microvisualization scanhead probe and analysis performed with its accompanying Vevo LAB 3.1.1 software (VisualSonics). The imaging was carried out at 7 days (right before the treatment) and 4 weeks post-MI. To assess contractility, cardiac strain analysis was performed through the longitudinal axis. The longitudinal endocardial strain at the time of AVC (representing end systole) in segment 6 (anterior apex segment), corresponding to the infarct zone area, was calculated. Results for both echocardiography and strain analyses were averaged from the analysis of two researchers blinded to the treatment groups.

Ex Vivo Imaging of Pep-5-PEG Hydrogel: The Pep-5-PEG hydrogel was labeled by adding Alexa-Fluor594 dye (25 nmol of dye per hydrogel) to the mixture prior to injection to the infarcted mouse heart, as described above. Animals were sacrificed at 2 and 7 days after treatment, and hearts were harvested and imaged *ex vivo* by IVIS Spectrum (PerkinElmer) to visualize Pep-5-PEG hydrogel retention within the hearts ($\lambda_{\text{excitation}}: 570 \text{ nm}$; $\lambda_{\text{emission}}: 640 \text{ nm}$).

Statistical Analysis: Statistical analysis was performed using KaleidaGraph or GraphPad Prism software. Statistically significant differences between more than two groups were determined by one-way ANOVA at a significance set at $p < 0.05$. Statistical significance of data with two groups

was performed using a two-tail unpaired *t*-test set at a $p < 0.05$. Data was reported as mean \pm standard deviation. Statistical analysis was performed using KaleidaGraph or GraphPad Prism software. Statistically significant differences between more than two groups were determined by one-way ANOVA at a significance set at $p < 0.05$. Statistical significance of data with two groups was performed using a two-tail unpaired *t*-test set at a $p < 0.05$. Data was reported as mean \pm standard deviation.

Supporting Information

Supporting Information is available from the Wiley Online Library or from the author.

Acknowledgements

This work was supported by grants from the Canadian Institutes of Health Research (CIHR) and Heart and Stroke Foundation of Canada to EIA and EJS. Funding support to EIA was also received from the Natural Sciences and Engineering Research Council (NSERC) and the Government of Ontario for an Early Career Research Award. EIA and EJS thank the support of INTBIOTECH-CREATE NSERC Canada. This work was also supported by the 3P University of Ottawa program to EIA and MR. AR was supported by a Graduate Scholarship from the University of Ottawa Cardiac Endowment Fund and an NSERC Doctoral Award. SDGS thanks MITACS Elevate funding and the University of Ottawa Heart Institute (UOHI) Foundation and the University of Ottawa Cardiac Endowment Fund for the strategic research Postdoctoral Fellowship. MM thanks the University of Ottawa Heart Institute, the Strategic Research Postdoctoral Fellowship, and the CIHR Fellowship MFE-186357. HP thanks a Fondecyt grant (#1211143) from ANID-Chile. The authors also thank Jianqun Wang (Carleton University) for his assistance in scanning electron microscopy (SEM) micrographs. Heat maps were generated using Tableau software. Peptides were synthesized in the Advanced Peptide Core Facility at University of Ottawa Heart Institute that was funded by NSERC-RTI and the Canadian Foundation for Innovation John R. Evans Leaders Fund. Schematics in Figures 1–4 and Graphical Abstract were created using BioRender. The authors would like to thank Drs. Ines Amara (University of Ottawa Heart Institute) and Mona Koaik (the Ottawa Hospital) for help on the CD206 staining and corneal curvature interpretation, respectively.

Conflict of Interest

A.R., X.G., A.G.M.S., S.D.G.S., M.C.B., I.G.S., A.M., M.M., M.R., E.J.S., and E.I.A. are listed as inventors in a patent application that describes the technology herein presented. The patent is owned by the University of Ottawa Heart Institute Research Corporation.

Author Contributions

A.R., X.G., and G.A.M.S. contributed equally to this work. E.I.A., M.R., E.J.S., M.G., J.L. performed study design. A.R., X.G., A.G.M.S., S.D.G.S., I.G.S., M.M., J.E.H., K.H., B.L., R.T., B.S., T.N., E.A., and B.R. performed peptide and material design, characterization, preparation, and *in vitro* testing. H.P., P.B.R. performed molecular simulations. J.E.H., A.G.M.S., M.C.B. performed handheld device design, fabrication, and optimization. A.R., X.G., A.G.M.S., H.T., and A.M. performed *In vivo* experimentation and data analysis. A.R., X.G., A.G.M.S., and A.M. performed histopathology studies. A.R., X.G., A.G.M.S., S.D.G.S., M.R., E.J.S., E.I.A. performed writing the first draft of the manuscript. All authors contributed to the article and revised sections of the manuscript.

Data Availability Statement

The data that support the findings of this study are openly available in FigShare at <https://figshare.com/s/f195a5a27cfc9072225>, reference number 24882327.

Keywords

biomimetic materials, peptides, regenerative therapies, soft tissue repair

Received: February 9, 2024

Revised: April 6, 2024

Published online:

- [1] A. Gaspar-Pintilie, A. M. Stanciu, O. Craciunescu, *Int. J. Biol. Macromol.* **2019**, *138*, 854.
- [2] M. N. Kantak, S. S. Bharate, *Carbohydr. Polym.* **2022**, *278*, 118999.
- [3] S. Bhat, A. Kumar, *Biomater* **2013**, *3*, 24717.
- [4] W. Zhang, L. Chen, J. Chen, L. Wang, X. Gui, J. Ran, G. Xu, H. Zhao, M. Zeng, J. Ji, L. Qian, J. Zhou, H. Ouyang, X. Zou, *Adv. Healthcare Mater.* **2017**, *6*, 1700121.
- [5] W. D. F. S. Spotnitz, *ISRN Surg* **2014**, *2014*, 1.
- [6] I. V. Roberts, D. Bukhary, C. Y. L. Valdivieso, N. Tirelli, *Macromol. Biosci.* **2020**, *20*, 1900283.
- [7] S. M. Willerth, S. E. Sakiyama-Elbert, in *StemBook* (Harvard Stem Cell Institute Copyright 2008 S. M. Willerth, S. E. Sakiyama-Elbert), **2008**.
- [8] E. Troy, M. A. Tilbury, A. M. Power, J. G. Wall, *Polymers (Basel)* **2021**, *13*, 3321.
- [9] S. Liu, J.-M. Yu, Y.-C. Gan, X.-Z. Qiu, Z.-C. Gao, H. Wang, S.-X. Chen, Y. Xiong, G.-H. Liu, S.-E. Lin, A. McCarthy, J. V. John, D.-X. Wei, H.-H. Hou, *Mil. Med. Res.* **2023**, *10*, 16.
- [10] G. Singh, A. Chanda, *Biomed. Mater.* **2021**, *16*, 062004.
- [11] M. S. Ganewatta, Z. Wang, C. Tang, *Nat Rev Chem* **2021**, *5*, 753.
- [12] S. Pascual-Gil, E. Garbayo, P. Díaz-Herráez, F. Prosper, M. J. Blanco-Prieto, *J. Controlled Release* **2015**, *203*, 23.
- [13] M. R. Caplan, E. M. Schwartzfarb, S. Zhang, R. D. Kamm, D. A. Lauffenburger, *Biomaterials* **2002**, *23*, 219.
- [14] M. A. Elsayy, J. K. Wychowaniec, L. A. Castillo Díaz, A. M. Smith, A. F. Miller, A. Saiani, *Biomacromolecules* **2022**, *23*, 2624.
- [15] D. V. Bax, N. Davidenko, D. Gullberg, S. W. Hamaia, R. W. Farndale, S. M. Best, R. E. Cameron, *Acta Biomater.* **2017**, *49*, 218.
- [16] W. N. Albrecht, R. L. Stephenson, *Scand J Work Environ Health* **1988**, *14*, 209.
- [17] S. Li, P. Wu, Z. Ji, Y. Zhang, P. Zhang, Y. He, Y. Shen, *J. Biomater. Sci., Polym. Ed.* **2023**, *34*, 482.
- [18] W. E. Hennink, C. F. van Nostrum, *Adv. Drug Delivery Rev.* **2002**, *54*, 13.
- [19] M. P. Lutolf, G. P. Raeber, A. H. Zisch, N. Tirelli, J. A. Hubbell, *Adv. Mater.* **2003**, *15*, 888.
- [20] C. Diaferia, E. Rosa, N. Balasco, T. Sibillano, G. Morelli, C. Giannini, L. Vitagliano, A. Accardo, *Chem. - Eur. J.* **2021**, *27*, 14886.
- [21] W. Y. Seow, G. Salgado, E. B. Lane, C. A. E. Hauser, *Sci. Rep.* **2016**, *6*, 32670.
- [22] M. M. Islam, R. Ravichandran, D. Olsen, M. K. Ljunggren, P. Fagerholm, C. J. Lee, M. Griffith, J. Phopase, *RSC Adv.* **2016**, *6*, 55745.
- [23] V. Kubyshev, *Org. Biomol. Chem.* **2019**, *17*, 8031.
- [24] T. McGraw, *Clin. Exp. Gastroenterol.* **2016**, *9*, 173.
- [25] C. E. Cooper, M. Bird, X. Sheng, J.-W. Choi, G. G. A. Silstone, M. Simons, N. Syrett, R. Piano, L. Ronda, S. Bettati, G. Paredi, A. Mozzarelli, B. J. Reeder, *Front. Chem.* **2021**, *9*, 707797.
- [26] S. P. Robins, *Biochem. Soc. Trans.* **2007**, *35*, 849.
- [27] D. P. Nair, M. Podgórski, S. Chatani, T. Gong, W. Xi, C. R. Fenoli, C. N. Bowman, *Chem. Mater.* **2014**, *26*, 724.
- [28] S. D. Fontaine, R. Reid, L. Robinson, G. W. Ashley, D. V. Santi, *Bioconjug. Chem.* **2015**, *26*, 145.
- [29] S. Ricard-Blum, *Cold Spring Harb. Perspect. Biol.* **2011**, *3*, a004978.
- [30] M. D. Shoulders, R. T. Raines, *Annu. Rev. Biochem.* **2009**, *78*, 929.
- [31] A. V. Persikov, J. A. M. Ramshaw, B. Brodsky, *J. Biol. Chem.* **2005**, *280*, 19343.
- [32] B. Brodsky, A. V. Persikov, in *Advances in Protein Chemistry*, Vol. 70, Academic Press, San Diego, CA **2005** pp. 301.
- [33] S. Cheng, T. Shi, X.-L. Wang, J. Liang, H. Wu, L. Xie, Y. Li, Y.-L. Zhao, *Mol. Biosyst.* **2014**, *10*, 2597.
- [34] S. Tsuda, S. Masuda, T. Yoshiya, *J. Org. Chem.* **2020**, *85*, 1674.
- [35] Y. Feng, G. Melacini, J. P. Taulane, M. Goodman, *J. Am. Chem. Soc.* **1996**, *118*, 10351.
- [36] G. Melacini, Y. Feng, M. Goodman, *J. Am. Chem. Soc.* **1996**, *118*, 10359.
- [37] T. Nagata, Y. Harada, M. Arai, T. Hirose, H. Kondo, *Transl. Vis. Sci. Technol.* **2020**, *9*, 24.
- [38] E. Natour, M. Suedkamp, O. E. Dapunt, *J. Cardiothorac. Surg.* **2012**, *7*, 105.
- [39] Y. Kim, S. O. Ho, N. R. Gassman, Y. Korlann, E. V. Landorf, F. R. Collart, S. Weiss, *Bioconjug. Chem.* **2008**, *19*, 786.
- [40] K. M. Meek, C. Knupp, *Prog. Ret. Eye Res.* **2015**, *49*, 1.
- [41] Y.-C. Chang, G. M. Mesquita, S. Williams, G. Gregori, F. Cabot, A. Ho, M. Ruggeri, S. H. Yoo, J.-M. Parel, F. Manns, *Biomed. Optics Exp.* **2019**, *10*, 411.
- [42] J. R. Suchard, *West J. Emerg. Med.* **2007**, *8*, 93.
- [43] H. H. Mitchell, T. S. Hamilton, F. R. Steggerda, H. W. Bean, *J. Biol. Chem.* **1945**, *158*, 625.
- [44] P. Asbell, D. Brocks, in *Encyclopedia of the Eye* (Ed: D. A. Dartt) Academic Press, San Diego **2010** pp. 522–531.
- [45] L. B. Boll, R. T. Raines, *ChemBiochem.* **2022**, *23*, 202200258.
- [46] G. Salgado, Y. Z. Ng, L. F. Koh, C. S. M. Goh, J. E. Common, *Differentiation* **2017**, *98*, 14.
- [47] C. M. Bhamidipati, J. S. Coselli, S. A. LeMaire, *J. Extra Corpor. Technol.* **2012**, *44*, P6.
- [48] H. Yuk, C. E. Varela, C. S. Nabzdyk, X. Mao, R. F. Padera, E. T. Roche, X. Zhao, *Nature* **2019**, *575*, 169.
- [49] Z. Ma, C. Bourquard, Q. Gao, S. Jiang, T. De lure-Grimmel, R. Huo, X. Li, Z. He, Z. Yang, G. Yang, Y. Wang, E. Lam, Z.-u.-H. Gao, O. Supponen, J. Li, *Science* **2022**, *377*, 751.
- [50] A. Wahlsten, A. Stracuzzi, I. Luchtefeld, G. Restivo, N. Lindenblatt, C. Giampietro, A. E. Ehret, E. Mazza, *Acta Biomater.* **2023**, *170*, 155.
- [51] C. D. McTiernan, D. C. Cortes, C. Lazurko, S. Amrani, R. Rosales-Rojas, M. Zuñiga-Bustos, V. Sedlakova, H. Poblete, K. Stamplecoskie, E. J. Suuronen, E. I. Alarcon, *ACS Appl. Mater. Interfaces.* **2019**, *11*, 45007.
- [52] A. J. MacAdam, M. Munoz, J. E. Hage, K. Hu, A. Ross, A. Chandra, J. D. Edwards, Z. Shahid, S. Mourcos, M. E. Comtois-Bona, A. Juarez, M. Groleau, D. S. Dégué, M. Djallali, M. Piché, M. Thériault, M. Grenier, M. Griffith, I. Brunette, E. I. Alarcon, *Adv. Funct. Mater.* **2023**, *33*, 2302721.
- [53] J. Heichel, F. Wilhelm, K. S. Kunert, T. Hammer, *Med. Hypothesis Discov. Innov. Ophthalmol.* **2016**, *5*, 125.
- [54] A. Sharma, N. Sharma, S. Basu, R. Sharma, S. Aggarwal, P. C. Gupta, J. Ram, V. S. Nirankari, *Clin. Ophthalmol.* **2023**, *17*, 209.
- [55] M. van de Vyver, K. Boodhoo, T. Frazier, K. Hamel, M. Kopcewicz, B. Levi, M. Maartens, S. Machcinska, J. Nunez, C. Pagani, E. Rogers, K. Walendzik, J. Wisniewska, B. Gawronska-Kozak, J. M. Gimble, *Stem Cells Dev.* **2021**, *30*, 1141.
- [56] R. Gund, R. Zirmire, Haarshaadri J, G. Kansagara, C. Jamora, *Bio-protoc* **2021**, *11*, e3894.
- [57] C. Lazurko, Z. Khatoon, K. Goel, V. Sedlakova, C. Eren Cimenci, M. Ahumada, L. Zhang, T.-F. Mah, W. Franco, E. J. Suuronen, E. I. Alarcon, *ACS Biomater. Sci. Eng.* **2020**, *6*, 1124.
- [58] S. McLaughlin, B. McNeill, J. Podrebarac, K. Hosoyama, V. Sedlakova, G. Cron, D. Smyth, R. Seymour, K. Goel, W. Liang, K. J. Rayner, M. Ruel, E. J. Suuronen, E. I. Alarcon, *Nat. Commun.* **2019**, *10*, 4866.

- [59] M. A. Cousin, A. J. Greenberg, T. H. Koep, D. Angius, M. J. Yaszemski, R. J. Spinner, A. J. Windebank, *Tissue Eng. Part B Rev.* **2016**, *22*, 430.
- [60] C. D. McTiernan, F. C. Simpson, M. Haagdorens, C. Samarawickrama, D. Hunter, O. Buznyk, P. Fagerholm, M. K. Ljunggren, P. Lewis, I. Pintelon, D. Olsen, E. Edin, M. Groleau, B. D. Allan, M. Griffith, *Sci. Adv.* **2020**, *6*, aba2187.
- [61] P. Lou, S. Liu, Y. Wang, C. Pan, X. Xu, M. Zhao, G. Liao, G. Yang, Y. Yuan, L. Li, J. Zhang, Y. Chen, J. Cheng, Y. Lu, J. Liu, *Acta Biomater.* **2021**, *135*, 100.
- [62] A. K. Nguyen, T. G. Molley, E. Kardia, S. Ganda, S. Chakraborty, S. L. Wong, J. Ruan, B. E. Yee, J. Mata, A. Vijayan, N. Kumar, R. D. Tilley, S. A. Waters, K. A. Kilian, *Nat. Commun.* **2023**, *14*, 6604.
- [63] R. Pugliese, F. Gelain, *Int. J. Mol. Sci.* **2020**, *21*, 4261.
- [64] M. P. Lutolf, J. A. Hubbell, *Biomacromolecules* **2003**, *4*, 713.
- [65] M. R. Reithofer, A. Lakshmanan, A. T. K. Ping, J. M. Chin, C. A. E. Hauser, *Biomaterials* **2014**, *35*, 7535.
- [66] M. Muttenthaler, G. F. King, D. J. Adams, P. F. Alewood, *Nat. Rev. Drug Discovery* **2021**, *20*, 309.
- [67] M. K. Mahapatra, M. Karuppasamy, B. M. Sahoo, *Rev. Endocr. Metab. Disord.* **2022**, *23*, 521.
- [68] T. Zhang, Z. Chen, Y. Tian, B. Han, N. Zhang, W. Song, Z. Liu, J. Zhao, J. Liu, *Org. Process Res. Dev.* **2015**, *19*, 1257.
- [69] B. L. Bray, *Nat. Rev. Drug Discovery* **2003**, *2*, 587.
- [70] L. Wang, N. Wang, W. Zhang, X. Cheng, Z. Yan, G. Shao, X. Wang, R. Wang, C. Fu, *Signal Transduct. Target. Ther.* **2022**, *7*, 48.
- [71] J. Levi, J. Wang, F. Venter, A. Hill, *Obesity* **2023**, *31*, 1270.
- [72] Y. Kuninaka, Y. Ishida, A. Ishigami, M. Nosaka, J. Matsuki, H. Yasuda, A. Kofuna, A. Kimura, F. Furukawa, T. Kondo, *Sci. Rep.* **2022**, *12*, 20327.
- [73] T. Takei, H. Nakahara, H. Ijima, K. Kawakami, *Acta Biomater.* **2012**, *8*, 686.
- [74] S. Das, D. Das, *Front. Chem.* **2021**, *9*, 4261.
- [75] R. Chen, C. Zhu, L. Xu, Yi Gu, S. Ren, H. Bai, Q. Zhou, X. Liu, S. Lu, X. Bi, W. Li, X. Jia, Z. Chen, *Biomaterials* **2021**, *274*, 120855.
- [76] Z. Fan, M. Fu, Z. Xu, B. Zhang, Z. Li, H. Li, X. Zhou, X. Liu, Y. Duan, P.-H. Lin, P. Duann, X. Xie, J. Ma, Z. Liu, J. Guan, *Biomacromolecules* **2017**, *18*, 2820.
- [77] K. M. Schultz, K. A. Kyburz, K. S. Anseth, *Proc. Natl. Acad. Sci. U.S.A.* **2015**, *112*, E3757.
- [78] A. V. Boopathy, M. D. Martinez, A. W. Smith, M. E. Brown, A. J. García, M. E. Davis, *Tissue Eng., Part A* **2015**, *21*, 2315.
- [79] L. Li, C. Lu, L. Wang, M. Chen, J. White, X. Hao, K. M. McLean, H. Chen, T. C. Hughes, *ACS Appl. Mater. Interfaces.* **2018**, *10*, 13283.
- [80] A. D'Souza, J. H. Yoon, H. Beaman, P. Gosavi, Z. Lengyel-Zhand, A. Sternisha, G. Centola, L. R. Marshall, M. D. Wehrman, K. M. Schultz, M. B. Monroe, O. V. Makhlynets, *ACS Appl. Mater. Interfaces.* **2020**, *12*, 17091.
- [81] D. E. Clarke, E. T. Pashuck, S. Bertazzo, J. V. M. Weaver, M. M. Stevens, *J. Am. Chem. Soc.* **2017**, *139*, 7250.
- [82] R. Li, C. Zhou, J. Chen, H. Luo, R. Li, D. Chen, X. Zou, W. Wang, *Bioact. Mater.* **2022**, *18*, 267.
- [83] R. B. Merrifield, *J. Am. Chem. Soc.* **1963**, *85*, 2149.
- [84] M. Mirdita, K. Schütze, Y. Moriwaki, L. Heo, S. Ovchinnikov, M. Steinegger, *Nat. Methods.* **2022**, *19*, 679.
- [85] J. Jumper, R. Evans, A. Pritzel, T. Green, M. Figurnov, O. Ronneberger, K. Tunyasuvunakool, R. Bates, A. Židek, A. Potapenko, A. Bridgland, C. Meyer, S. A. A. Kohl, A. J. Ballard, A. Cowie, B. Romera-Paredes, S. Nikolov, R. Jain, J. Adler, T. Back, S. Petersen, D. Reiman, E. Clancy, M. Zielinski, M. Steinegger, M. Pacholska, T. Berghammer, S. Bodenstein, D. Silver, O. Vinyals, et al., *Nature* **2021**, *596*, 583.
- [86] S. R. Eddy, *PLoS Comput. Biol.* **2011**, *7*, 1002195.
- [87] M. Steinegger, M. Mirdita, J. Söding, *Nat. Methods.* **2019**, *16*, 603.
- [88] J. Pupkaite, M. Ahumada, S. McLaughlin, M. Temkit, S. Alaziz, R. Seymour, M. Ruel, I. Kochevar, M. Griffith, E. J. Suuronen, E. I. Alarcon, *ACS Appl. Mater. Interfaces.* **2017**, *9*, 9265.
- [89] K. Vanommeslaeghe, E. Hatcher, C. Acharya, S. Kundu, S. Zhong, J. Shim, E. Darian, O. Guvench, P. Lopes, I. Vorobyov, A. D. Mackerell, *J. Comput. Chem.* **2010**, *31*, 671.
- [90] C. W. Hopkins, S. Le Grand, R. C. Walker, A. E. Roitberg, *J. Chem. Theory Comput.* **2015**, *11*, 1864.
- [91] S. E. Feller, Y. Zhang, R. W. Pastor, B. R. Brooks, *J. Chem. Phys.* **1995**, *103*, 4613.
- [92] G. Fiorin, M. L. Klein, J. Hénin, *Mol. Phys.* **2013**, *111*, 3345.
- [93] P. Coussot, S. Boyer, *Rheol. Acta* **1995**, *34*, 534.
- [94] P. Moller, A. Fall, V. Chikkadi, D. Derks, D. Bonn, *Phil. Trans.* **2009**, *367*, 5139.
- [95] T. Yasuda, K. Shimokasa, *J. Text. Studies* **2022**, *53*, 307.
- [96] R. Aston, K. Sewell, T. Klein, G. Lawrie, L. Grøndahl, *Eur. Pol. J.* **2016**, *82*, 1.
- [97] F04.05, Standard Test Method for Wound Closure Strength of Tissue Adhesives and Sealants; ASTM F2458. **2015**.
- [98] D. Ghosh, C. M. Salinas, S. Pallod, J. Roberts, I. R. S. Makin, J. R. Yaron, R. S. Witte, K. Rege, *Bioeng. Transl. Med.* **2023**, *8*, 10412.
- [99] G. F. Caetano, M. Fronza, M. N. Leite, A. Gomes, M. A. C. Frade, *Pharm. Biol.* **2016**, *54*, 2555.
- [100] M. E. Comtois-Bona, A. Chandra, J. E. I. Hage, B. Liu, S. David Garcia-Schejtman, A. J. MacAdam, I. Brunette, M. Munoz, E. I. Alarcon, *Adv. Eng. Mater.* **2023**, *25*, 2300695.